

# Intervalence Charge Transfer Luminescence: Interplay between anomalous and $5d - 4f$ emissions in Yb-doped fluorite-type crystals.

Zoila Barandiarán<sup>1,2,\*</sup> and Luis Seijo<sup>1,2</sup>

<sup>1</sup>Departamento de Química, Universidad Autónoma de Madrid, 28049 Madrid, Spain

<sup>2</sup>Instituto Universitario de Ciencia de Materiales Nicolás Cabrera,

Universidad Autónoma de Madrid, 28049 Madrid, Spain

(Dated: November 24, 2014)

In this paper we report the existence of intervalence charge transfer (IVCT) luminescence in Yb-doped fluorite-type crystals associated with  $\text{Yb}^{2+}\text{-Yb}^{3+}$  mixed valence pairs. By means of embedded cluster, wave function theory *ab initio* calculations, we show that the widely studied, very broad band, anomalous emission of  $\text{Yb}^{2+}$ -doped  $\text{CaF}_2$  and  $\text{SrF}_2$ , usually associated with impurity-trapped excitons, is, rather, an IVCT luminescence associated with  $\text{Yb}^{2+}\text{-Yb}^{3+}$  mixed valence pairs. The IVCT luminescence is very efficiently excited by a two-photon upconversion mechanism where each photon provokes the same strong  $4f^{14}\text{-}1A_{1g}\text{-}4f^{13}(^2F_{7/2})5de_g\text{-}1T_{1u}$  absorption in the  $\text{Yb}^{2+}$  part of the pair: the first one, from the pair ground state; the second one, from an excited state of the pair whose  $\text{Yb}^{3+}$  moiety is in the higher  $4f^{13}(^2F_{5/2})$  multiplet. The  $\text{Yb}^{2+}\text{-Yb}^{3+} \rightarrow \text{Yb}^{3+}\text{-Yb}^{2+}$  IVCT emission consists of an  $\text{Yb}^{2+} 5de_g \rightarrow \text{Yb}^{3+} 4f_{7/2}$  charge transfer accompanied by a  $4f_{7/2} \rightarrow 4f_{5/2}$  deexcitation within the  $\text{Yb}^{2+} 4f^{13}$  subshell:  $[^2F_{5/2}5de_g, ^2F_{7/2}] \rightarrow [^2F_{7/2}, 4f^{14}]$ . The IVCT vertical transition leaves the oxidized and reduced moieties of the pair after electron transfer very far from their equilibrium structures; this explains the unexpectedly large band width of the emission band and its low peak energy, because the large reorganization energies are subtracted from the normal emission. The IVCT energy diagrams resulting from the quantum mechanical calculations explain the different luminescent properties of Yb-doped  $\text{CaF}_2$ ,  $\text{SrF}_2$ ,  $\text{BaF}_2$ , and  $\text{SrCl}_2$ : the presence of IVCT luminescence in Yb-doped  $\text{CaF}_2$  and  $\text{SrF}_2$ ; its coexistence with regular  $5d\text{-}4f$  emission in  $\text{SrF}_2$ ; its absence in  $\text{BaF}_2$  and  $\text{SrCl}_2$ ; the quenching of all emissions in  $\text{BaF}_2$ ; and the presence of additional  $5d\text{-}4f$  emissions in  $\text{SrCl}_2$  which are absent in  $\text{SrF}_2$ . They also allow to interpret and reproduce recent experiments on transient photoluminescence enhancement in  $\text{Yb}^{2+}$ -doped  $\text{CaF}_2$  and  $\text{SrF}_2$ , the appearance of  $\text{Yb}^{2+} 4f\text{-}5d$  absorption bands in the excitation spectra of the IR  $\text{Yb}^{3+}$  emission in partly reduced  $\text{CaF}_2\text{:Yb}^{3+}$  samples, and to identify the broad band observed in the excitation spectrum of the so far called anomalous emission of  $\text{SrF}_2\text{:Yb}^{2+}$  as an IVCT absorption, which corresponds to an  $\text{Yb}^{2+} 4f_{5/2} \rightarrow \text{Yb}^{3+} 4f_{7/2}$  electron transfer.

Keywords: *Ab initio*, IVCT, electron transfer,  $\text{Yb}^{2+}$ ,  $\text{Yb}^{3+}$ , fluorites, anomalous emission, luminescence

## I. INTRODUCTION

The capability of lanthanide ion dopants to luminesce from their  $4f^N$  and/or  $4f^{N-1}5d$  excited states has granted them a prominent role as activators in solid state lighting, lasers, fiber amplifiers, and medical imaging devices.<sup>1-4</sup> Frequently, however, their applicability is compromised by quenching or by replacement of the expected luminescence by an anomalous emission. Detailed understanding of these mechanisms is important in the search for new interesting phosphor and scintillating materials based on lanthanide ion activators.

The anomalous emission of  $\text{Yb}^{2+}$  in Yb-doped materials is a prototypical case (for a review on the anomalous emission of  $\text{Yb}^{2+}$  and  $\text{Eu}^{2+}$ -doped crystals, see Ref. 5). The interplay between anomalous and  $5d\text{-}4f$  emissions in  $\text{Yb}^{2+}$ -doped fluorite-type crystals results in a complex electronic spectroscopy, which has been the focus of investigations for decades.<sup>5-14</sup> The adjective anomalous has been used to reflect the irregular, unexpected, very large Stokes shift of the emission observed, with respect to the  $4f^{14} \rightarrow 4f^{13}5d$  excitation, which makes the red shifted emission band extremely broad. When  $\text{Yb}^{2+}$  is doped in  $\text{CaF}_2$ , the anomalous emission prevails;<sup>6-8,11,13</sup> it also occurs in  $\text{SrF}_2$ , where both, anomalous emission and regular  $4f^{13}5d \rightarrow 4f^{14}$  luminescence have been detected together;<sup>8-10,14</sup> and no emission

whatsoever occurs in  $\text{BaF}_2$  up to  $1.5\mu\text{m}$ .<sup>8,11</sup> Changing the ligand, as in the  $\text{SrF}_2$  and  $\text{SrCl}_2$  series, also affects the interplay. The dual character of the luminescence of Yb in  $\text{SrF}_2$  disappears in the  $\text{SrCl}_2$  host, where the anomalous emission is not observed; only regular  $5d\text{-}4f$  emission bands have been assigned in this case showing a complex temperature behaviour.<sup>15,16</sup> Analyses of spectroscopic data have suggested that the anomalous emission observed in  $\text{Yb}^{2+}$ -doped  $\text{CaF}_2$  and  $\text{SrF}_2$  is associated with an excited state which has a "radically different" (smaller) radiative rate compared with that of higher lying levels.<sup>11,13</sup> This characteristic has allowed the application of a two-frequency UV + IR transient photoluminescence enhancement technique which ultimately produces the IR excited state absorption spectrum (ESA) from the lowest anomalous state to close lying energy levels.<sup>13,14</sup> The anomalous emission of Yb has also been observed in  $\text{Yb}^{3+}$ -doped  $\text{CaF}_2$  after application of reducing conditions.<sup>12</sup>

Analogous competitions between regular  $5d\text{-}4f$  (as well as  $4f\text{-}4f$ ) and anomalous emissions have been reported involving other commonly used lanthanide ion activators:  $\text{Ce}^{3+}$ ,  $\text{Pr}^{3+}$ , and  $\text{Eu}^{2+}$ .<sup>5,8,9,17-19</sup> For all of them (including  $\text{Yb}^{2+}$ ), it is recognized that it is difficult to prevent the coexistence of another different valence state,<sup>8,15,16,20-23</sup> which means that the formation of mixed valence pairs, that is, pairs between two metal sites differing only in oxidation

state, is very likely. In this way, occurrence of  $Ce^{3+}-Ce^{4+}$ ,  $Pt^{3+}-Pt^{4+}$ ,  $Eu^{2+}-Eu^{3+}$ , and  $Yb^{2+}-Yb^{3+}$  mixed valence pairs should be expected, to some extent. In this paper we show that the study of the electronic structure of  $Yb^{2+}-Yb^{3+}$  mixed valence pairs is crucial to understand anomalous emission and its interplay with regular emissions in Yb-doped fluorite-type crystals. The same is true for  $Ce^{3+}-Ce^{4+}$  pairs, as we show in an analogous study of the anomalous emission in  $Ce^{3+}$ -doped  $Cs_2LiLuF_6$  elpasolite.<sup>24</sup>

Since mixed valence pairs (for lanthanides:  $Ln^{n+}-Ln^{(n+1)+}$ ) constitute a donor-acceptor (DA) redox system, electron transfer between the donor and acceptor sites,  $Ln^{n+} + Ln^{(n+1)+} \rightarrow Ln^{(n+1)+} + Ln^{n+}$ , may occur, and the process can be referred to as an intervalence charge transfer (IVCT),<sup>25</sup> in analogy with the IVCT processes that have been investigated involving mostly mixed valence transition metal compounds<sup>26-30</sup> and, scarcely, lanthanide ions.<sup>31,32</sup> Although most IVCT studies refer to thermally and radiatively induced electron transfer between the ground states of the donor and acceptor sites, we show here that the  $D + A \rightarrow A + D$  reaction can involve many of the excited electronic states of the mixed valence pair and lead to a variety of non-radiative and radiative IVCT processes.

The goal of this paper is to show that all of the spectral features we have summarized above for  $Yb^{2+}$ -doped  $CaF_2$ ,  $SrF_2$ ,  $BaF_2$ , and  $SrCl_2$  hosts can be explained if the existence of  $Yb^{2+}-Yb^{3+}$  mixed valence pairs is assumed, *ab initio* multielectronic wavefunction-based diabatic potential energy surfaces of the ground and excited states of the embedded  $Yb^{2+}-Yb^{3+}$  active pairs are calculated, and quantitative energy diagrams for the  $Yb^{2+} + Yb^{3+} \rightarrow Yb^{3+} + Yb^{2+}$  electron transfer reaction, along well defined reaction coordinates, are produced. In this framework, the anomalous emission of Yb-doped fluorite-type crystals is interpreted as an  $Yb^{2+}-Yb^{3+} \rightarrow Yb^{3+}-Yb^{2+}$  IVCT emission, in which an  $Yb^{2+} 5d_{e_g} \rightarrow Yb^{3+} 4f_{7/2}$  electron transfer and a  $4f_{7/2} \rightarrow 4f_{5/2}$  deexcitation within the  $Yb^{2+} 4f^{13}$  subshell take place:  $[^2F_{5/2}5d_{e_g}, ^2F_{7/2}] \rightarrow [^2F_{7/2}, 4f^{14}]$ . So, the bielectronic character of this IVCT luminescence explains the very slow radiative decay rate of the so far called anomalous emission. Its very large band width comes from the large change in the electron transfer reaction coordinate accompanying the electronic transition:  $|\Delta Q_{et}| = 0.49 \text{ \AA}$  ( $CaF_2$ ),  $0.60 \text{ \AA}$  ( $SrF_2$ ). Its occurrence and temperature quenching in  $CaF_2$  and  $SrF_2$ , including its coexistence with regular  $5d-4f$  emission in  $SrF_2$  below 140 K, or its absence in  $BaF_2$  and  $SrCl_2$ , including the absence of any emission in  $BaF_2$ , can be understood on the basis of changes in the topology of the diabatic IVCT energy diagrams of the  $Yb^{2+}-Yb^{3+}$  intervalence pairs in the different hosts. The IR ESA spectra measured in  $CaF_2$  and  $SrF_2$  are also reproduced, showing a close, upper lying state, which may contribute a much faster monolectronic  $Yb^{2+} 5d_{e_g} \rightarrow Yb^{3+} 4f_{5/2}$  IVCT emission, plus a number of other close lying upper levels which contribute to the transient photoluminescence enhancement.

In parallel to this work, we are presenting analogous studies on the nature of the anomalous luminescence of Ce-doped  $Cs_2LiLuCl_6$  and its interplay with regular emissions.<sup>24</sup> There, the fast anomalous emission of Ce is identified as a monolectronic  $Ce^{3+} 5d_{e_g} \rightarrow Ce^{4+} 4f$  IVCT luminescence, which is observed and calculated to be above the lowest, regular  $5d_{e_g} \rightarrow 4f$  emission of the  $Ce^{3+}$  active center. That work and the present paper are part of an effort focused on assessing and showing the relevance of intervalence charge transfer processes in the optical properties of very common lanthanide ions activators. Both works show that IVCT luminescence has been observed experimentally, but has not been identified as such, neither in  $Yb^{2+}$ -doped nor in  $Ce^{3+}$ -doped crystals. The same is true for other IVCT processes which are predicted and have not been identified or observed (i.e. transient IVCT photoluminescence enhancement, other IVCT absorptions, emissions, and non-radiative energy transfers). Altogether, the results presented so far suggest that the theoretical effort should continue and cover other common hosts and activators like those mentioned above; they also suggest that incorporating quantitative IVCT energy diagrams to experimental analyses should be useful.<sup>33</sup>

This paper is organized as follows: In Sec. II we describe the *ab initio* calculation of intervalence charge transfer potential energy surfaces of  $Yb^{2+}-Yb^{3+}$  pairs in fluorite-type crystals and the corresponding IVCT configuration coordinate diagrams. In Sec. III we interpret the anomalous luminescence of  $CaF_2:Yb^{2+}$  as an IVCT luminescence, we explain its mechanism and we discuss the involvement of IVCT states in transient photoluminescence enhancement experiments and in the excitation of the IR  $Yb^{3+}$  emission by  $Yb^{2+} 4f-5d$  absorptions. Finally, in Sec. IV we show that changes in the topology of the IVCT energy diagrams account for the interplay between IVCT and regular  $5d-4f$  emissions in the chemical series of fluorite-type crystals  $CaF_2$ ,  $SrF_2$ ,  $BaF_2$  (Sec. IV A) and  $SrF_2$ ,  $SrCl_2$  (Sec. IV B). The conclusions are summarized in Sec. V.

## II. POTENTIAL ENERGY SURFACES OF $YB^{2+}-YB^{3+}$ ACTIVE PAIRS IN FLUORITE-TYPE CRYSTALS

In this Section we describe how the diabatic potential energy surfaces of the ground and excited states of  $Yb^{2+}-Yb^{3+}$  mixed valence active pairs can be calculated in the  $CaF_2$ ,  $SrF_2$ ,  $BaF_2$ , and  $SrCl_2$  ( $MX_2$ ) hosts using the potential energy surfaces obtained from independent  $Yb^{2+}$  and  $Yb^{3+}$  embedded cluster calculations as building blocks. From them, quantitative IVCT energy diagrams can be built in terms of normal electron transfer reaction coordinates which involve concerted vibrational breathing modes of the donor ( $YbX_8$ )<sup>6-</sup> and acceptor ( $YbX_8$ )<sup>5-</sup> sites. The approximations involved in this procedure are outlined; their accuracy is expected to be sufficient to achieve the goals of this work, which have been stated in the Introduction.

### A. $\text{Yb}^{2+}\text{-Yb}^{3+}$ diabatic potential energy surfaces

A convenient definition for the diabatic wavefunctions and energies of the  $\text{Yb}^{2+}\text{-Yb}^{3+}$  mixed valence pairs can be set up using generalized antisymmetric product functions<sup>34</sup> resulting from the combination of the  $n_D$  states of the donor  $D$ , and  $n_A$  states of the acceptor  $A$  sites, which in this work are the states of the  $4f^{14}$ ,  $4f^{13}5de_g$ ,  $4f^{13}5dt_{2g}$ , and  $4f^{13}a_{1g}^{ITE}$  manifolds of the donor  $(\text{YbX}_8)^{6-}$  and those of the  $4f^{13}$  manifold of the acceptor  $(\text{YbX}_8)^{5-}$  separated embedded clusters, respectively. So, from the combination of the state  $i$  of  $D$ ,  $\Phi_{Di}$ , and the state  $j$  of  $A$ ,  $\Phi_{Aj}$ , two diabatic wavefunctions are obtained: one for the  $ij$  state of  $DA$ ,  $M\hat{A}(\Phi_{Di}\Phi_{Aj})$ , and one for the  $ji$  state of  $AD$ ,  $M\hat{A}(\Phi_{Aj}\Phi_{Di})$  ( $M$  is a normalization constant and  $\hat{A}$  is the inter-group antisymmetrization operator<sup>34</sup>), where  $DA$  and  $AD$  refer to the mixed valence pairs before and after electron transfer:  $\text{Yb}^{2+}\text{-Yb}^{3+}$  and  $\text{Yb}^{3+}\text{-Yb}^{2+}$ , respectively. These two diabatic wavefunctions will be needed to study the electron transfer  $(\text{YbX}_8)_L^{6-} - (\text{YbX}_8)_R^{5-} \rightarrow (\text{YbX}_8)_L^{5-} - (\text{YbX}_8)_R^{6-}$  from the left to the right moieties of the mixed valence pair embedded in the  $\text{MX}_2$  solid. Altogether, a basis of  $2n_D n_A$  diabatic wavefunctions are obtained. The two corresponding diabatic potential energy surfaces  $E_{DiAj}^{\text{diab}}$  and  $E_{AjDi}^{\text{diab}}$  are the expected values of the fixed nuclei Hamiltonian of the embedded pair  $\hat{H}$ :  $E_{DiAj}^{\text{diab}} = \langle M\hat{A}(\Phi_{Di}\Phi_{Aj}) | \hat{H} | M\hat{A}(\Phi_{Di}\Phi_{Aj}) \rangle$ ,  $E_{AjDi}^{\text{diab}} = \langle M\hat{A}(\Phi_{Aj}\Phi_{Di}) | \hat{H} | M\hat{A}(\Phi_{Aj}\Phi_{Di}) \rangle$ . Given that the electronic spectroscopic transitions are dominated by the totally symmetric vibrational coordinates, the breathing modes of the donor  $(\text{YbX}_8)^{6-}$  and acceptor  $(\text{YbX}_8)^{5-}$  sites are the only vibrational degrees of freedom we will consider, which results in the parametric dependence of the diabatic potential energy surfaces on the Yb–X distance in the left and right components of the  $DA$  and  $AD$  pairs,  $d_L$  and  $d_R$ :  $E_{DiAj}^{\text{diab}}(d_L, d_R)$  and  $E_{AjDi}^{\text{diab}}(d_L, d_R)$ . Note that  $E_{DiAj}^{\text{diab}}(x, y) = E_{AjDi}^{\text{diab}}(y, x)$ . The two diabatic potential energy surfaces for the ground state 00 of the  $\text{Yb}^{2+}\text{-Yb}^{3+}$  mixed valence pair in Yb-doped  $\text{CaF}_2$ ,  $E_{D0A0}^{\text{diab}}(d_L, d_R)$  and  $E_{A0D0}^{\text{diab}}(d_L, d_R)$ , can be seen in Fig. 1.

It is important to note that in this work the electronic coupling between any two diabatic states  $ij$  of  $DA$  and  $kl$  of  $AD$ ,  $V_{DiAj, kDl}^{\text{diab}} = \langle M\hat{A}(\Phi_{Di}\Phi_{Aj}) | \hat{H} | M\hat{A}(\Phi_{kD}\Phi_{lD}) \rangle$ , will be neglected for all values of the  $d_L$  and  $d_R$  coordinates. As a consequence, there will be no avoided crossings among the diabatic potential energy surfaces nor mixings between the diabatic states. Whereas this approximation can be expected to be a good one away from the intersection regions, it becomes weaker on them, since the diabatic energies at intersections give upperbounds to the energy barriers that would result from avoided crossings should the electronic couplings be considered. We comment further on this issue in the next section where diabatic energy diagrams for the electron transfer reactions will be extracted from the diabatic energy surfaces. As we will show in this work, many spectroscopic features of the mixed valence pairs can be addressed quantitatively or semiquantitatively within the

diabatic approximation, using the diabatic energy surfaces only. We describe next how they will be computed in this work.

According to the group function theory used to define the diabatic wavefunctions of the mixed valence pairs, the diabatic pair energies are the sum of the donor and acceptor energies plus their mutual Coulomb and exchange interaction.<sup>34</sup> The latter should be almost independent of the donor and acceptor states, in general. Hence, we can write:

$$E_{DiAj}^{\text{diab}} = E_{Di} + E_{Aj} + E_{DiAj}^{\text{cx}} \approx E_{Di} + E_{Aj} + E_{DA}^{\text{cx}}. \quad (1)$$

In Eq. 1,  $E_{Di}$  and  $E_{Aj}$  include the embedding interactions of  $D$  and  $A$  with the crystalline environment of the  $DA$  pair in the  $\text{MX}_2$  crystal. In this work, we will compute  $E_{DiAj}^{\text{diab}}$  using the energy curves obtained from independent donor  $(\text{YbX}_8)^{6-}$  and acceptor  $(\text{YbX}_8)^{5-}$  clusters embedded in the perfect  $\text{MX}_2$  hosts, as building blocks. According to this alternative we will use:

$$E_{DiAj}^{\text{diab}}(d_L, d_R) = E_{Di}^{(\text{iec})}(d_L) + E_{Aj}^{(\text{iec})}(d_R) + E_0^{(\text{iec})}(d_{DA}),$$

$$E_{AjDi}^{\text{diab}}(d_L, d_R) = E_{Aj}^{(\text{iec})}(d_L) + E_{Di}^{(\text{iec})}(d_R) + E_0^{(\text{iec})}(d_{DA}), \quad (2)$$

where  $E_{Di}^{(\text{iec})}(d_L)$  and  $E_{Aj}^{(\text{iec})}(d_L)$  are the independent embedded cluster energy curves of the donor and acceptor obtained as described in Sec. II B, and

$$E_0^{(\text{iec})}(d_{DA}) = E_{DA}^{\text{cx}}(d_{DA}) - E_{DM}^{\text{cx}}(d_{DA}) - E_{AM}^{\text{cx}}(d_{DA})$$

$$\approx (q_D \times q_A - (q_D + q_A) \times q_M) e^2 / d_{DA}, \quad (3)$$

with  $E_{DM}^{\text{cx}}$  (or  $E_{AM}^{\text{cx}}$ ) standing for the Coulomb and exchange interaction energy between the donor  $(\text{YbX}_8)^{6-}$  (or acceptor  $(\text{YbX}_8)^{5-}$ ) cluster and the cluster of the original host cation  $(\text{MX}_8)^{6-}$  ( $M$ :  $\text{Ca}^{2+}$ ,  $\text{Sr}^{2+}$ , or  $\text{Ba}^{2+}$ , in this case). Except for short cation-cation distances,  $-E_{DM}^{\text{cx}} - E_{AM}^{\text{cx}} + E_{DA}^{\text{cx}} \approx (-q_D \times q_M - q_A \times q_M + q_D \times q_A) e^2 / d_{DA} = (-2 \times 2 - 3 \times 2 + 2 \times 3) e^2 / d_{DA} = -(2 \times 2) e^2 / d_{DA}$ . In any case, the term  $E_0^{(\text{iec})}(d_{DA})$  is common to the  $DA$  and  $AD$  energy surfaces and to all states of both. Its effect is a common shift of all of them and, consequently, it does not contribute to energy differences between them.

In this alternative, the symmetry reductions around  $D$  and  $A$  due to the presence of the other ( $A$  and  $D$ , respectively) are not considered. Therefore, the energy splittings driven by symmetry lowering, which are dependent on the distance and relative orientation between  $D$  and  $A$ , are not obtained. The most important ones in the present work would be the splittings produced on the  $(\text{YbX}_8)^{6-}$  levels by the presence of the  $\text{Yb}^{3+}$  substitutional ion. Yet, whereas such site symmetry reductions would add significant computational effort to the embedded cluster calculations, the corresponding splittings would only be responsible for fine structure features of the spectra; they would neither affect the positions nor the number of the main absorption and emission bands. Therefore, the alternative chosen in this work will be able to capture the basics of the energy surfaces of the pairs by means of completely independent calculations on the  $D$  and  $A$  embedded clusters. This is the strength of the present approach.

## B. Independent embedded cluster calculations

In this Section we describe the details and summarize the results of the quantum mechanical calculations of the  $E_{Di}(d_{Yb-X})$  and  $E_{Aj}(d_{Yb-X})$  components of the mixed valence pair energies in Eq. 2. As donor  $D$  and acceptor  $A$  we adopted, respectively, the  $(YbX_8)^{6-}$  and  $(YbX_8)^{5-}$  clusters ( $X = F, Cl$ ). We performed *ab initio* wave function theory embedded cluster quantum chemical calculations on these clusters embedded in the  $MX_2$  hosts, with the MOLCAS suite of programs.<sup>35</sup> The calculations include bonding interactions, static and dynamic electron correlation effects, and scalar and spin-orbit coupling relativistic effects within the clusters, which are treated at a high theoretical level. They also include Coulomb, exchange, and Pauli repulsion interactions between the host and the clusters, which are considered at a lower theoretical level by means of a quantum mechanical embedding potential. Electron correlation effects between the cluster and the host are excluded from these calculations.

### 1. Details of the quantum mechanical calculations

The calculations presented here assume that  $Yb^{2+}$  and  $Yb^{3+}$  ions substitute for  $M^{2+}$  ( $M^{2+} = Ca^{2+}, Sr^{2+}, Ba^{2+}$ ) and occupy cubic sites in the perfect fluorite structures.<sup>36</sup> Following the embedded-cluster approximation, the imperfect crystals were divided into the defect cluster and the embedded host, which were represented as follows.

The embedded-cluster scalar relativistic second-order Douglas-Kroll-Hess Hamiltonian<sup>37,38</sup> and wave functions, comprising the Yb impurity at (0,0,0) and eight X ligands at variable (x,x,x), included all the electrons of  $Yb^{2+}$  or  $Yb^{3+}$  and eight  $X^-$ . The basis sets used to expand the cluster molecular orbitals included the all electron ANO-RCC bases Yb (25s22p15d11f4g2h) [9s8p5d4f3g2h], F (14s9p4d3f2g) [5s4p3d] or Cl (17s12p5d4f2g) [6s5p3d].<sup>39,40</sup> In addition, the highest occupied  $s$  and  $p$  orbitals of the embedding  $M^{2+}$  ions, contracted as  $Ca^{2+}$  (20s15p)[1s1p],  $Sr^{2+}$  (23s19p)[1s1p],  $Ba^{2+}$  (27s23p)[1s1p], were used as orthogonalization functions at the 12 second neighbour sites  $(\frac{1}{2}, \frac{1}{2}, 0)$ , to fulfil strong orthogonality, and 5  $s$ -type Gaussian type functions were used at the six  $(\frac{1}{2}, 0, 0)$  interstitial sites surrounding the  $YbX_8$  cube in the fluorite structures; their orbital exponents were optimized to give minimal impurity-trapped exciton energy. The embedded-cluster calculations were performed using  $D_{2h}$  symmetry.

AIMP embedding potentials were used in the embedded-cluster Hamiltonian to represent the host effects due to interactions with the remainder of the crystal ions, which include quantum mechanical embedding effects associated with exchange and Pauli repulsion, in addition to Coulomb electron repulsion and Madelung interactions.<sup>41,42</sup> The embedding potentials for all four  $MX_2$  hosts were obtained in this work to represent the  $M^{2+}$  and  $X^-$  ions located outside

the cluster, at their cubic crystal structure sites [Group 225,  $Fm\bar{3}m$ ,  $a_0 = 5.46294 \text{ \AA}$  ( $CaF_2$ ),  $5.796 \text{ \AA}$  ( $SrF_2$ ),  $6.2001 \text{ \AA}$  ( $BaF_2$ ),  $6.9744 \text{ \AA}$  ( $SrCl_2$ )<sup>36</sup>]; the potentials were obtained by performing self-consistent embedded  $M^{2+}$  and  $F^-$  ions calculations at the Hartree-Fock level on the perfect host crystal as described in Ref. 42. All ions located in a cube of  $7 \times 7 \times 7$  unit cells, centered at the impurity site, were represented by their total ion embedding AIMP; an additional set of 2781 point charges was used to ensure that the Ewald potential is reproduced within the cluster volume. These charges were obtained following the zero multipole method of Gellé and Le Petit.<sup>43</sup>

A recent study on radial correlation effects on interconfigurational transitions at the end of the lanthanide series has revealed that  $4f$  to  $5f$  double excitations must be included at the variational multiconfigurational self-consistent field step preceding second order perturbation theory calculations.<sup>44</sup> Consequently, state-average restricted active space self-consistent field (RASSCF)<sup>45-47</sup> calculations were done on the  $(YbX_8)^{6-}$  and  $(YbX_8)^{5-}$  embedded clusters including  $4f$  to  $5f$  single and double excitations from the  $4f^{14}$  and  $4f^{13}$  reference to calculate the  $4f^{14-1}A_{1g}$  ground state, and the  ${}^2A_{2u}$ ,  ${}^2T_{1u}$ , and  ${}^2T_{2u}$  states of the  $4f^{13}$  manifold, whereas single excitations from the  $4f^{14}$  reference to one  $a_{1g}$  shell and to the  $5d$  shell (which belong to the  $e_g$  and  $t_{2g}$   $O_h$  irreducible representations) were also allowed to provide the minimal configurational space required for the spectroscopy of the  $(YbX_8)^{6-}$  cluster, plus additional single and double excitations from the  $4f$  shell to the  $5f$  shell to account for the large change of radial correlation upon  $4f^{14} \rightarrow 4f^{13}5d^1$  electronic transitions. These calculations are referred here as RASSCF( $4f-3h/5f/a_{1g}e_g t_{2g}-1e$ ), which indicates the maximum number of holes allowed in the  $4f^{14}$  shell and the maximum number of electrons allowed in the empty  $a_{1g}$  and  $5d$  shells to calculate the *ungerade*  ${}^{2S+1}\Gamma_u$  states of the  $\Gamma = A_{1u}, A_{2u}, E_u, T_{1u}, T_{2u}$  octahedral irreps.

Once these wave functions are obtained, they become the multireference for multistate second order perturbation theory calculations (MS-RASPT2),<sup>47-49</sup> which include dynamic electron correlation, also necessary for getting sufficient precision in the structure and electronic transition data. At this level, all valence electrons of the embedded-cluster were correlated, which amounts to 86 and 85 electrons (Yb: 22 or 21; eight X: 64). We used the standard IPEA parameter value (0.25 a.u.) introduced in Ref. 50 as a simple way to correct for systematic underestimations of CASPT2 transition energies from closed-shell ground states to open-shell excited states, also recommended for other cases. An imaginary shift of 0.1 was also used to avoid intruder states.<sup>51</sup>

The highly correlated wavefunctions and energies resulting from the previous spin-orbit free step, namely, the eigenvectors (which are transformed RASSCF wave functions) and eigenvalues (MS-RASPT2 energies) of the spin-orbit free effective Hamiltonian computed at the MS-RASPT2 step, were transferred and used in the last step of

spin-orbit coupling calculations, which used the restricted-active-space state interaction method (RASSI-SO).<sup>52</sup> The transformed RASSCF wave functions were used to compute the spin-orbit coupling matrix resulting from adding the AMFI approximation of the Douglas-Kroll-Hess spin-orbit coupling operator<sup>53</sup> to the scalar relativistic Hamiltonian. Given that  $D_{2h}$  symmetry was used, the MS-RASPT2 energies show slight degeneracy breakings which would spread further throughout the spin-orbit calculation. Hence, the spin-free-state-shifting technique was used to substitute them for averaged values which were used in the diagonal elements of the spin-orbit coupling matrix. The calculation and diagonalization of the transformed RASSCF spin-orbit interaction matrix leads to the final results of the *ab initio* calculations on the independent  $(\text{YbX}_8)^{6-}$  and  $(\text{YbX}_8)^{5-}$  active centers, which can be used in Eq. 2 to compute the diabatic potential energy surfaces of the  $(\text{YbX}_8)^{6-}-(\text{YbX}_8)^{5-}$  mixed valence active pairs.

The program MOLCAS was used for all calculations.<sup>35</sup> All AIMP data (for embedding and/or for cores) and interstitial basis set can be found in Ref. 54.

## 2. Energy curves of $\text{Yb}^{2+}$ and $\text{Yb}^{3+}$ independent active centers

The results of the quantum mechanical calculations on the donor  $(\text{YbX}_8)^{6-}$  and acceptor  $(\text{YbX}_8)^{5-}$  cubic clusters embedded in the four  $\text{MX}_2$  hosts are collected in the Supplementary Material of this paper, where the details of the electronic structure of the ground and excited states of the  $\text{Yb}^{2+}$  and  $\text{Yb}^{3+}$  active centers are presented.<sup>55</sup> Tables I to IV of Ref. 55 include the Yb-X equilibrium bond distance, totally symmetric vibrational frequency, minimum-to-minimum energy differences relative to the  $4f^{14}-1A_{1g}$  ground state, and analyses of the spin-orbit wavefunctions of all  $7A_{1u}$ ,  $7A_{2u}$ ,  $14E_u$ ,  $21T_{1u}$ , and  $21T_{2u}$  spin-orbit levels calculated. They also include the results for the electronic states of the  $4f^{13}$  configuration of the  $\text{Yb}^{3+}$  active centers. Plots of their energy curves vs. the Yb-X bond distance at different levels of methodology (RASSCF, MS-RASPT2, and RASSI-SO) and the calculated absorption spectra are also presented in Figures 1 to 5 of Ref. 55. The data of only the lowest levels (14 of  $\text{Yb}^{2+}$  and 5 of  $\text{Yb}^{3+}$ ) in  $\text{CaF}_2$  are presented here in Table I; selected energy curves are presented in the left graphs of Fig. 2; all the energy curves are presented in the left graph of Fig. 3.

The excited states of  $\text{Yb}^{2+}$  in the four hosts appear to be grouped in four manifolds of impurity states (see Table I and left graph of Fig. 3 for  $\text{CaF}_2$ ):  $4f^{13}(7/2)5de_g$ ,  $4f^{13}(5/2)5de_g$ ,  $4f^{13}(7/2)5dt_{2g}$ , and  $4f^{13}(5/2)5dt_{2g}$ , and two of impurity-trapped excitons (ITE):  $4f^{13}(7/2)a_{1g}^{YbTE}$  and  $4f^{13}(5/2)a_{1g}^{YbTE}$ , which, in some cases, show significant configurational interaction. The more delocalized ITE states, whose electronic structure shows the same characteristics as those found in previous quantum mechanical studies on  $\text{U}^{4+}$ -doped  $\text{Cs}_2\text{GeF}_6$ ,<sup>56</sup> and  $\text{Yb}^{2+}$ -doped  $\text{SrCl}_2$ ,<sup>57</sup> appear above the lowest  $4f^{13}(7/2)5de_g$  impurity manifold

in all four hosts. The lowest excited states of  $\text{Yb}^{2+}$  are, in all cases, the  $4f^{13}(7/2)5de_g$  electric dipole forbidden  $1E_u$ ,  $1T_{2u}$ , and the electric dipole allowed  $1T_{1u}$  states. (In all figures, blue and green colours have been used for the energy curves of the  $4f^{13}5de_g$  and  $4f^{13}5dt_{2g}$  manifolds, respectively; maroon has been used when they interact among themselves or with ITE states. Black has been used for the  $\text{Yb}^{2+}$  ground state and for the lowest  $4f^{13}(7/2)$  manifold of  $\text{Yb}^{3+}$ ; red is used for the higher  $4f^{13}(7/2)$  components.)

The present *ab initio* results and those of calculations presented elsewhere,<sup>58</sup> especially designed to allow the wavefunctions of excited states to spread electron density beyond first neighbours, over the twelve next  $\text{Ca}^{2+}$  or  $\text{Sr}^{2+}$  ions, as proposed by McClure and Pédrini for impurity-trapped excitons,<sup>9,11</sup> allow to conclude that none of the electronic states of the  $\text{Yb}^{2+}$  active centers can be considered responsible for the anomalous emission observed in the  $\text{CaF}_2$  and  $\text{SrF}_2$  hosts. Therefore, the hypothesis of the impurity-trapped excitons being responsible for the anomalous emission<sup>9,11</sup> is not supported by the *ab initio* quantum mechanical calculations. Impurity-trapped excitons show up in the calculations, but at much higher energies than those that would allow them to play a role in the anomalous emission. As we show in Sec.III and IV, intervalence charge transfer within the  $\text{Yb}^{2+}-\text{Yb}^{3+}$  active pairs has to be invoked instead.

## C. Quantitative energy diagrams for $\text{Yb}^{2+}-\text{Yb}^{3+}$ intervalence charge transfer reaction

Even though the calculation of the two diabatic potential energy surfaces  $E_{DiAj}^{\text{diab}}(d_L, d_R)$  and  $E_{AjDi}^{\text{diab}}(d_L, d_R)$  associated with each  $ij$  state of the embedded pair before and after electron transfer is necessary for the obtention of the structural and energetic results discussed in this paper (note that any of the  $\text{MX}_2:\text{Yb}^{2+}-\text{Yb}^{3+}$  excited states lead to two energy surfaces like those for the ground state presented in Fig. 1, which would make their joint plot extremely crowded and cumbersome), the extraction of the minimal energy electron transfer reaction path from them is a very important step leading to quantitative IVCT energy diagrams which will be actually used to discuss IVCT luminescence and other radiative and non-radiative IVCT processes in Sec. III and IV. In this Section we explain how these diagrams are built: In a first step, the normal electron transfer reaction coordinate  $Q_{et}$  for the ground state of the mixed valence pair,  $Q_{et}^{00}$ , will be defined from the topology of the  $E_{D0A0}^{\text{diab}}(d_L, d_R)$  and  $E_{A0D0}^{\text{diab}}(d_L, d_R)$  energy surfaces, in terms of concerted vibrational breathing modes of the donor  $D$  and acceptor  $A$  sites, which leads to the diabatic  $E_{D0A0}^{\text{diab}}(Q_{et}^{00})$  and  $E_{A0D0}^{\text{diab}}(Q_{et}^{00})$  branches for the reaction. In a second step, the energy curves of the excited states of the mixed valence pairs will be evaluated at the  $d_L, d_R$  coordinate values which correspond to the  $Q_{et}^{00}$  axis, leading to  $E_{DiAj}^{\text{diab}}(Q_{et}^{00})$  and  $E_{AjDi}^{\text{diab}}(Q_{et}^{00})$  branches for all states of interest and, hence, to the final quantitative IVCT diagram. The same procedure would be applicable to any

other two  $E_{DiAj}^{\text{diab}}(d_L, d_R)$  and  $E_{AjDi}^{\text{diab}}(d_L, d_R)$  diabatic surfaces, which would lead to analogous energy diagrams along corresponding  $Q_{et}^{ij}$  reaction coordinates.

### 1. Electron transfer reaction coordinate

Within the diabatic approximation, the two symmetric diabatic energy surfaces involved in the electron transfer reaction between the  $D$  and  $A$  ground states,  $E_{D0A0}^{\text{diab}}(d_L, d_R)$  and  $E_{A0D0}^{\text{diab}}(d_L, d_R)$ , do intersect, without avoiding crossing, at all  $d_L = d_R$  points (see Fig. 1), where they are degenerate, while the corresponding pair wavefunctions  $M\hat{A}(\Phi_{D0}\Phi_{A0})$  and  $M\hat{A}(\Phi_{A0}\Phi_{D0})$  never mix, but keep their pure character. In this way, the electron transfer reaction path (see Fig. 1, top right graph) connects the energy minimum of the  $DA$   $(\text{YbX}_8)_L^{6-}-(\text{YbX}_8)_R^{5-}$  pair,  $E_{e,00}=E_{D0A0}^{\text{diab}}(d_{eD}, d_{eA})$ , for which the  $(\text{YbX}_8)_L^{6-}$  and  $(\text{YbX}_8)_R^{5-}$  clusters are at their Yb–X equilibrium distance,  $d_L = d_{eD}$  and  $d_R = d_{eA}$ , with that of the symmetrical minimum of the  $AD$   $(\text{YbX}_8)_L^{5-}-(\text{YbX}_8)_R^{6-}$  pair,  $E_{e,00}=E_{A0D0}^{\text{diab}}(d_{eA}, d_{eD})$ , at the  $d_L = d_{eA}$ ,  $d_R = d_{eD}$  point, crossing from the  $DA$  to the  $AD$  surface through the activated complex, which is the crossing point with minimal energy, equal sharing of the transferred electron, and equal Yb–X bond distance for the left and right clusters of the  $DA$  and  $AD$  pairs,  $d_L = d_R = d_{ac}$ . The diabatic electron transfer activation energy:  $E_{D0A0}^{\# \text{diab}} = E_{D0A0}^{\text{diab}}(d_{ac}, d_{ac}) - E_{e,00}$ , is an upperbound to the energy barrier that would result from avoided crossings should the electronic coupling between the two energy surfaces be considered. Whereas the diabatic activation energy is independent from the distance between the  $D$  and  $A$  moieties of the pairs,  $d_{DA}$ , the adiabatic energy barrier is  $d_{DA}$ -dependent. As commented above, it is close to the activated complex structure where the diabatic approximation is weakest.

The ground state diabatic reaction coordinate  $Q_{et}$  (for simplicity we will drop the superscript in  $Q_{et}^{00}$  from now on) can be approximated with the straight lines that connect the activated complex  $(d_{ac}, d_{ac})$  with the two minima  $(d_{eD}, d_{eA})$  and  $(d_{eA}, d_{eD})$ . This reaction coordinate is represented in Fig. 1 in the  $d_L-d_R$  plane. The  $DA$  pair has the lowest diabatic energy in the left side of the activation complex ( $d_L > d_R$ ) and the  $AD$  pair in the right side ( $d_L < d_R$ ), in correspondance with the larger size of  $D$  at equilibrium. Since these lines contain the most interesting information of the diabatic energy surfaces, it is convenient to plot them in energy diagrams along the reaction coordinate:  $E_{DiAj}^{\text{diab}}(Q_{et})$  and  $E_{AjDi}^{\text{diab}}(Q_{et})$  instead of the more cumbersome  $(d_L, d_R)$ -dependent energy surfaces,  $E_{D0A0}^{\text{diab}}(d_L, d_R)$  and  $E_{A0D0}^{\text{diab}}(d_L, d_R)$ , as mentioned above.

For a precise definition of  $Q_{et}$ , we can recall that the changes of the Yb–X distances in the left and right clusters  $d_L$  and  $d_R$  along the reaction coordinate fulfil

$$d_L - d_{ac} = m(d_R - d_{ac}) \begin{cases} m = \frac{d_{eD} - d_{ac}}{d_{eA} - d_{ac}} : d_L \geq d_R \\ m = \frac{d_{eA} - d_{ac}}{d_{eD} - d_{ac}} : d_L \leq d_R \end{cases} \quad (4)$$

Then, the normal reaction coordinate can be written as

$$Q_{et} = \frac{1}{\sqrt{1+m^2}} (Q_R + mQ_L), \quad (5)$$

$Q_L$  and  $Q_R$  being the normal breathing modes of the left and right  $\text{YbX}_8$  moieties with respect to their structures in the activated complex:

$$Q_L = \frac{1}{\sqrt{8}} (\delta_{X_{L1}} + \delta_{X_{L2}} + \dots + \delta_{X_{L8}}), \\ Q_R = \frac{1}{\sqrt{8}} (\delta_{X_{R1}} + \delta_{X_{R2}} + \dots + \delta_{X_{R8}}), \quad (6)$$

which have been expressed in terms of the displacements  $\delta_{X_{Lk}}$  and  $\delta_{X_{Rk}}$  of the X ligand atoms in the left and right  $\text{YbX}_8$  moieties away from their respective Yb atoms, starting from the positions they occupy in the activated complex. A graphical representation of the X displacements along  $Q_{et}$  is shown in Fig. 1 (bottom graph). Since the left and right cluster breathings imply  $\delta_{X_{L1}} = \delta_{X_{L2}} = \dots = d_L - d_{ac}$  and  $\delta_{X_{R1}} = \delta_{X_{R2}} = \dots = d_R - d_{ac}$ , we can write

$$Q_L = \sqrt{8}(d_L - d_{ac}), \\ Q_R = \sqrt{8}(d_R - d_{ac}), \quad (7)$$

and

$$Q_{et} = \sqrt{\frac{8}{1+m^2}} [(d_R - d_{ac}) + m(d_L - d_{ac})] \\ = \sqrt{8(1+m^2)}(d_R - d_{ac}) \\ = \sqrt{8(1+m^2)}(d_L - d_{ac})/m. \quad (8)$$

We may mention the relationship of this reaction coordinate and the one of the vibronic model of Piepho *et al.*<sup>30</sup> The latter corresponds to  $d_{qc} = (d_{eD} + d_{eA})/2$ , which implies  $m = -1$  and gives  $Q_{et} = \frac{1}{\sqrt{2}}(Q_R - Q_L) = 2(d_R - d_L)$ .

### 2. Quantitative $\text{Yb}^{2+}-\text{Yb}^{3+}$ IVCT energy diagrams

According to Eq. 2 and Eqs. 4–8, quantitative IVCT energy diagrams for the embedded  $\text{Yb}^{2+}-\text{Yb}^{3+}$  active pairs can be obtained using the energy curves resulting from the independent embedded cluster calculations of the electronic states of the donor  $(\text{YbX}_8)^{6-}$  and acceptor  $(\text{YbX}_8)^{5-}$  active centers described in Sec. II B. We illustrate here how this is done using the energy curves of only two electronic states for the donor and acceptor clusters embedded in  $\text{CaF}_2$ , ( $n_D = 2, n_A = 2$ ): the ground state and one excited state, which have been plotted in the left graph of Fig. 2. The IVCT energy diagram resulting from them, which includes  $2n_D n_A = 8$  diabatic mixed valence pair states, is plotted in the right graph of Fig. 2 and is described next. The much more dense IVCT energy diagrams used below in this paper result from obvious extensions which use the

complete manifold of excited states calculated for the separated active centers.

Using the energy curves of the  $1A_{1g}$  and  $1\Gamma_{7u}$  ground states of the  $Yb^{2+}$  and  $Yb^{3+}$  doped  $CaF_2$  (see Table I), the diabatic potential energy surfaces  $E_{D_0A_0}^{diab}(d_L, d_R)$  and  $E_{A_0D_0}^{diab}(d_L, d_R)$ , for the pair before  $(YbX_8)_L^{6-}-(YbX_8)_R^{5-}$  [ $1A_{1g}, 1\Gamma_{7u}$ ] and after  $(YbX_8)_L^{5-}-(YbX_8)_R^{6-}$  [ $1\Gamma_{7u}, 1A_{1g}$ ] electron transfer, are obtained from Eq. 2. From any of them, the activated complex structure,  $d_{ac}=2.261 \text{ \AA}$ , is obtained searching for the minimal energy along the  $d_L = d_R$  axis. Using this value, plus the Yb-F equilibrium distances of the independent embedded cluster ground states,  $d_{eD}=2.329 \text{ \AA}$  ( $1A_{1g}$ ) and  $d_{eA}=2.201 \text{ \AA}$  ( $1\Gamma_{7u}$ ), respectively, the diabatic electron transfer reaction coordinate for the ground state of the mixed valence pair is defined from Eqs. 4–8, and the two mixed valence pair ground state branches [ $1A_{1g}, 1\Gamma_{7u}$ ] and [ $1\Gamma_{7u}, 1A_{1g}$ ] are obtained; they are plotted in black in the right graph of Fig. 2. The two diabatic energy curves cross at the activated complex structure ( $Q_{et}=0 \text{ \AA}$ ;  $d_L = d_R = 2.261 \text{ \AA}$ ;  $E_{D_0A_0}^{#diab}=3774 \text{ cm}^{-1}$ ). In the structures of the pair around the minimum of the  $DA$  state [ $1A_{1g}, 1\Gamma_{7u}$ ] ( $Q_{et}=-0.256 \text{ \AA}$ ;  $d_L = d_{eD}=2.329$ ,  $d_R = d_{eA}=2.201 \text{ \AA}$ ), the complementary  $AD$  state [ $1\Gamma_{7u}, 1A_{1g}$ ] has a much higher energy because the oxidized and reduced moieties,  $A$  and  $D$ , are under strong structural stress. The opposite is true around the minimum of the  $AD$  state [ $1\Gamma_{7u}, 1A_{1g}$ ]. We indicate this in the energy diagram by representing the energy of a given mixed valence pair state with full lines when it is around its minimum, and with dashed lines when it is under strong stress. Computing the energies of the excited states of the pairs at the  $d_L, d_R$  values corresponding to the ground state electron transfer coordinate we obtained the energy curves of the  $DA$  states [ $1A_{1g}, 2\Gamma_{7u}$ ] (red), [ $1E_u, 1\Gamma_{7u}$ ] (blue), and [ $1E_u, 2\Gamma_{7u}$ ] (orange), plus their IVCT  $AD$  counterparts. They are plotted in the right graph of Fig. 2 using the above definition of solid and dashed lines.

The quantitative IVCT diagram shown in Fig. 2 can be used to read different types of processes.

The  $D_0A_0 \rightarrow A_0D_0$  thermally induced ground state intervalence electron transfer reaction,  $Yb^{2+}-Yb^{3+}$  [ $1A_{1g}, 1\Gamma_{7u}$ ]  $\rightarrow$   $Yb^{3+}-Yb^{2+}$  [ $1\Gamma_{7u}, 1A_{1g}$ ], with an upperbound activation energy barrier of  $3774 \text{ cm}^{-1}$  (black, solid line connecting the two equivalent ground state minima through the activated complex).

Vertical absorptions of the independent active centers, which occur at their (fixed) ground state structure, such as: the  $Yb^{3+}$   $4f-4f$  absorption  $1\Gamma_{7u} \rightarrow 2\Gamma_{7u}$ , at a  $Yb^{3+}$ -F distance  $2.201 \text{ \AA}$  ( $D_0A_0 \rightarrow D_0A_1$ , arrow 1), and the  $Yb^{2+}$   $4f-5d$  absorption  $1A_{1g} \rightarrow 1E_u$ , at a  $Yb^{2+}$ -F distance  $2.329 \text{ \AA}$  ( $D_0A_0 \rightarrow D_1A_0$ , arrow 2). These transitions are the same read in the energy curves of the independent active centers in the left graph of Fig. 2.

Vertical IVCT absorptions from the pair ground state, at fixed  $Q_{et}=-0.256 \text{ \AA}$ , which means a left Yb-F distance  $2.329 \text{ \AA}$  and a right Yb-F distance  $2.201 \text{ \AA}$ . The initial pair

$(YbX_8)_L^{6-}-(YbX_8)_R^{5-}$  is relaxed and, after the radiatively induced electron transfer, the final pair  $(YbX_8)_L^{5-}-(YbX_8)_R^{6-}$  is very stressed and far from equilibrium. These absorption bands are very wide. There is a lowest IVCT absorption ( $D_0A_0 \rightarrow A_0D_0$ , arrow 3), which leads to the photoinduced ground state electron transfer reaction after non-radiative decay, and higher lying IVCT absorptions, like  $D_0A_0 \rightarrow A_0D_1$  (arrow 4).

Electron transfer non-radiative decays to the ground state or to excited states of the pair can also be visualized in the IVCT energy diagram, like the  $D_0A_1 \rightarrow A_0D_0$  or the  $D_1A_0 \rightarrow A_1D_0$  decays. In this cases, although the IVCT diagram is very helpful identifying the most probable decay mechanisms, the corresponding energy barriers have to be found in the full diabatic potential energy surfaces involved,  $E_{D_1A_1}^{diab}(d_L, d_R)$  and  $E_{A_1D_1}^{diab}(d_L, d_R)$ , because they may occur at  $d_L, d_R$  points not corresponding to the ground state electron transfer reaction coordinate  $Q_{et}$  axis.

Finally, vertical emissions can also be discussed using the IVCT energy diagrams in analogous terms as we have discussed vertical absorptions above. These can be regular emissions of the independent active centers, like  $A_1D_0 \rightarrow A_0D_0$  (arrow 5), and IVCT emissions, like  $A_1D_1 \rightarrow D_0A_0$  (arrow 6). Rigorously, the electron transfer reaction coordinate  $Q_{et}$  axis should correspond to the  $ij$  emitting state of the pair. Yet, the IVCT diagram obtained for the  $Q_{et}^{00}$  and  $Q_{et}^{ij}$  axes are very similar in most cases. Hence, although the transition energies tabulated in this work will be calculated rigorously, we will use the ground state IVCT energy diagram to discuss absorption, decays, and emission processes altogether. Therefore, independent active center emissions and IVCT emissions will be discussed in analogous terms as the independent active center absorptions and IVCT absorptions, with obvious substitutions of the  $Q_{et}$  fixed values involved in the radiative processes and their effects on the emission band structure.

### III. IVCT LUMINESCENCE IN $CaF_2:Yb^{2+}$

In this Section we present and discuss in detail the IVCT luminescence of  $CaF_2:Yb^{2+}$ . The manifolds of excited states of  $Yb^{2+}-Yb^{3+}$  pairs in  $CaF_2$  are introduced in Sec. III A and they are used to interpret the anomalous luminescence of  $CaF_2:Yb^{2+}$  as an IVCT luminescence in Sec. III B, where its mechanism is discussed in detail. Additionally, we discuss two experiments that reinforce the involvement of IVCT states: Firstly, in Sec. III C we show that the transient photoluminescence enhancement measured via two-frequency excitation experiments can be interpreted, in detail, as an IVCT photoluminescence enhancement experiment; then, in Sec. III D we show that the IVCT model also explains the excitation of the IR  $Yb^{3+}$  emission by  $Yb^{2+}$   $4f-5d$  absorptions.

### A. Excited states of $\text{Yb}^{2+}-\text{Yb}^{3+}$ pairs

The full diabatic IVCT energy diagram for the ground and excited states of the  $\text{Yb}^{2+}-\text{Yb}^{3+}$  pairs in  $\text{CaF}_2$ , along the normal reaction coordinate of the ground state, can be seen in Fig. 3. It has been built using all the parent independent embedded cluster energy curves plotted in the left graph, following the procedure explained in Section II C 2. The vertical transition energies from the  $\text{Yb}^{2+}-\text{Yb}^{3+}$  [ $1A_{1g}, 1\Gamma_{7u}$ ] ground state minimum ( $Q_{et} = -0.256$ ,  $d_L, d_R = 2.330, 2.201$  Å; zero energy in the diagram), which can be read directly from the diagram, are also collected in Table II. As indicated in the Table, only the excited states which are relevant for the discussions of this paper have been tabulated; the remaining data is available in Ref. 55. Vertical transition energies from the minima of other two electronic states of the  $\text{Yb}^{2+}-\text{Yb}^{3+}$  pairs, [ $1A_{1g}, 2\Gamma_{7u}$ ] and [ $2A_{1u}, 1\Gamma_{7u}$ ], have also been included in Table II. In the [ $1A_{1g}, 2\Gamma_{7u}$ ] state the  $(\text{YbX}_8)^{5-}$  right moiety of the  $\text{Yb}^{2+}-\text{Yb}^{3+}$  pair is excited in the lowest of the  $4f^{13}(5/2)$  levels; in the [ $2A_{1u}, 1\Gamma_{7u}$ ] state the  $(\text{YbX}_8)^{6-}$  left moiety is excited in the lowest of  $4f^{13}(5/2)5d_e$  levels (cf. symmetry labels and configurational character of the parent independent embedded cluster states in Table I). Vertical absorptions and emissions from their minima will be used in the next subsections; however, their values cannot be read directly from the IVCT diagram of Fig. 3, since its electron transfer reaction coordinate is that of the ground state. Specific IVCT diagrams along the [ $1A_{1g}, 2\Gamma_{7u}$ ] and [ $2A_{1u}, 1\Gamma_{7u}$ ] reaction coordinates would have to be constructed using Eqs. 4–8 and the procedure outlined in Sec. II C 2. However, the similarity of all three IVCT diagrams allows to visualize the data from Table II in Fig. 3.

Diabatic energy barriers for the IVCT reaction  $\text{Yb}^{2+}-\text{Yb}^{3+} \rightarrow \text{Yb}^{3+}-\text{Yb}^{2+}$ , connecting two different electronic states of the pairs:  $[D_i, A_j] \rightarrow [A_k, D_l]$ , have been included in Table III for the forward and backwards reactions, together with the  $d_L, d_R$  coordinates of their activated complex point, since they play an important role in non-radiative decay pathways, as discussed below. The forward/backwards energy barriers have been calculated searching for the activated complex point of the  $[D_i, A_j] \rightarrow [A_k, D_l]$  reaction directly along the intersection points of the two  $E_{D_i A_j}^{\text{diab}}(d_L, d_R)$  and  $E_{A_k D_l}^{\text{diab}}(d_L, d_R)$  energy surfaces. Again, even though the activated complex  $d_L, d_R$  structures gathered in the Table do not necessarily fall in the ground state electron transfer reaction coordinate of Fig. 3, they are not far from the crossing points of their respective  $E_{D_i A_j}^{\text{diab}}(Q_{et})$  and  $E_{A_k D_l}^{\text{diab}}(Q_{et})$  branches; so, they can be visualized in Fig. 3.

In the following and for clarity, the IVCT energy diagram of Fig. 3 will be reduced so as to include only the electronic states that have been found to participate in the IVCT luminescence mechanism of Yb-doped  $\text{CaF}_2$  crystals and in the electronic spectroscopy experiments that will be discussed below. The reduced IVCT diagram appears in Fig. 4.

### B. IVCT luminescence mechanism

The results of the quantum mechanical calculations described in the preceding sections suggest that the IVCT luminescence, which has been observed experimentally and has been interpreted so far as an *anomalous* luminescence, occurs according to the following mechanism involving steps I to V. The data which characterize the radiative and non-radiative processes the  $\text{Yb}^{2+}-\text{Yb}^{3+}$  pair states undergo, can be found in Table II and Fig. 4; Table I should be useful to clarify the electronic structure of their  $\text{Yb}^{2+}$  and  $\text{Yb}^{3+}$  parent states.

#### 1. Step I. First photon absorption.

Step I is the first photon absorption [ $1A_{1g}, 1\Gamma_{7u}$ ]  $\rightarrow$  [ $1T_{1u}, 1\Gamma_{7u}$ ].

This step is the lowest electric dipole allowed  $4f^{14} \rightarrow 4f^{13}5d_e$  excitation of  $\text{Yb}^{2+}$ :  $1A_{1g} \rightarrow 1T_{1u}$ .<sup>20,21</sup> Temperature dependent (multiphonon) non-radiative decay to the lowest lying state of the  $4f^{13}5d_e$  configuration,  $1E_u$ , can be expected to occur.<sup>16,59</sup> Alternatively, a lower energy photon can excite directly the  $1E_u$  state with a less efficient, electric dipole forbidden transition.<sup>11</sup> These two states can be labelled as the [ $1T_{1u}, 1\Gamma_{7u}$ ] and [ $1E_u, 1\Gamma_{7u}$ ] states of the  $\text{Yb}^{3+}-\text{Yb}^{2+}$  pair, respectively. Comparisons between their calculated vertical transition energies and experimental peak energies<sup>6,7,21</sup> (Table II, 25706  $\text{cm}^{-1}$  and 23576  $\text{cm}^{-1}$  vs. 27400  $\text{cm}^{-1}$  and 24814  $\text{cm}^{-1}$ , respectively), suggest similar overestimations of around 1500  $\text{cm}^{-1}$ .

#### 2. Step II. Non-radiative electron transfer

Step II is the non-radiative electron transfer [ $1T_{1u}, 1\Gamma_{7u}$ ] and/or [ $1E_u, 1\Gamma_{7u}$ ]  $\rightarrow$  [ $2\Gamma_{7u}, 1A_{1g}$ ].

A very small energy barrier (49  $\text{cm}^{-1}$ ) is found for  $\text{Yb}^{2+}-\text{Yb}^{3+}$  [ $1T_{1u}, 1\Gamma_{7u}$ ] to  $\text{Yb}^{3+}-\text{Yb}^{2+}$  [ $2\Gamma_{7u}, 1A_{1g}$ ] electron transfer, which suggests that such non-radiative decay is very likely to occur. At the activated complex point of the electron transfer,  $(d_L, d_R) = (2.323$  Å,  $2.197$  Å) the resulting  $\text{Yb}^{3+}-\text{Yb}^{2+}$  [ $2\Gamma_{7u}, 1A_{1g}$ ] state is so structurally stressed that a profound non-radiative relaxation towards its final equilibrium structure  $(d_L, d_R) = (2.201$  Å,  $2.330$  Å) follows (see step II in Fig. 4). The same is true for the [ $1E_u, 1\Gamma_{7u}$ ]  $\rightarrow$  [ $2\Gamma_{7u}, 1A_{1g}$ ] non-radiative charge transfer for which the energy barrier is found to be even smaller: 14  $\text{cm}^{-1}$ .

These small energy barriers suggest that step II, which is an  $\text{Yb}^{2+}(^2F_{7/2}5d_e) - \text{Yb}^{3+}(^2F_{7/2}) \rightarrow \text{Yb}^{3+}(^2F_{5/2}) - \text{Yb}^{2+}(4f^{14})$  non-radiative IVCT that leaves  $\text{Yb}^{3+}$  in its  $^2F_{5/2} 2\Gamma_{7u}$  excited state, should be an efficient quenching mechanism for regular  $4f^{13}5d_e \rightarrow 4f^{14}$  radiative emissions back to the ground state. This explains that experimental detection of these emissions has never been reported for the  $\text{CaF}_2$  host, as far as we know.



Going into more details, it is worth noticing that  $[1E_u, 1\Gamma_{7u}]$  can excite the IVCT directly through non-radiative decay along step II, followed by steps III and IV explained below.  $[1T_{1u}, 1\Gamma_{7u}]$ , however, can excite it directly through its own step II, but also indirectly through an intermediate decay to  $[1E_u, 1\Gamma_{7u}]$ . This explains the difference observed experimentally in the short time part of the intensity decay curves of the anomalous (IVCT) emission: whereas the intensity of the emission shows a risetime when  $1T_{1u}$  is excited, the risetime disappears when  $1E_u$  is directly excited instead.<sup>11</sup>

The calculations show branching of the step II non-radiative decays, which could result in quenching of the IVCT luminescence. Besides, the energy barrier for the electron transfer reaction back to the ground state of the  $Yb^{2+}-Yb^{3+}$  pair after step II,  $Yb^{3+}-Yb^{2+} [2\Gamma_{7u}, 1A_{1g}] \rightarrow Yb^{2+}-Yb^{3+} [1A_{1g}, 1\Gamma_{7u}]$ , is found to be  $285 \text{ cm}^{-1}$ . All this indicate that: (i) both non-radiative decays below the branching should occur, and (ii) the pairs that decay to the  $Yb^{3+}-Yb^{2+} [2\Gamma_{7u}, 1A_{1g}]$  minimum (the end of step II) and can yield IVCT luminescence after the next steps, will still face temperature dependent decay to the ground state through the low energy barrier. This is in agreement with the fact that quenching of the anomalous luminescence of  $\text{CaF}_2:\text{Yb}^{2+}$  has been observed at  $180 \text{ K}$ .<sup>11,60</sup> Also, since the temperature dependence of the non-radiative decay from the  $1T_{1u}$  to the  $1E_u$  states of  $Yb^{2+}$  mentioned in step I,  $[1T_{1u}, 1\Gamma_{7u}] \rightarrow [1E_u, 1\Gamma_{7u}]$ , should influence step II as well, right at the initiation of the IVCT emission mechanism, the overall temperature dependence of the IVCT luminescence should be complex; this is further discussed in Sec. IV A 2.

### 3. Step III. Second photon absorption.

Step III is the second photon absorption  $[2\Gamma_{7u}, 1A_{1g}] \rightarrow [2\Gamma_{7u}, 1T_{1u}]$ .

This step is equivalent to step I, since  $Yb^{2+}$  is excited to its lowest  $4f^{14} \rightarrow 4f^{13}5de_g$  electric dipole allowed level  $1T_{1u}$  by a second photon of the same wavelength as that of step I. The difference is that now, after step II, the  $Yb^{3+}$  component of the pair is in its  ${}^2F_{5/2} \ 2\Gamma_{7u}$  excited state instead of its  ${}^2F_{7/2} \ 1\Gamma_{7u}$  ground state. As commented in step I, alternatively, the lower lying  $[2\Gamma_{7u}, 1E_u]$  state can be directly excited in this step by a second, lower energy photon.

This step reveals that the excitation of the IVCT luminescence is a two-photon process. Whether excitation of the yellow-green anomalous luminescence is a one- or a two-photon process has not been investigated experimentally, as far as we know.

### 4. Step IV. Non-radiative decay to the luminescent level.

Step IV is the non-radiative decay to the luminescent level  $[2\Gamma_{7u}, 1T_{1u}] \rightarrow [1\Gamma_{7u}, 2A_{1u}]$ .

The non-radiative relaxation from  $[2\Gamma_{7u}, 1T_{1u}]$  to the lowest  $[1\Gamma_{7u}, 2A_{1u}]$  level in this energy region separated from lower lying states by a large energy gap, is now significantly different from that described in step I after excitation to the  $[1T_{1u}, 1\Gamma_{7u}]$  state with the first photon, because the number and nature of the electronic states that are found below the excited level are now different. In effect, the first photon excites to the lowest levels of the  $Yb^{2+}-Yb^{3+} [{}^2F_{7/2}5de_g, {}^2F_{7/2}]$  manifold, in which both the  $4f^{13}$  inner-shell of  $Yb^{2+}$  and the  $4f^{13}$  shell of  $Yb^{3+}$  are in their  ${}^2F_{7/2}$  ground spin-orbit multiplet. However, the second photon excites to a more crowded energy region, where two manifolds of the  $Yb^{3+}-Yb^{2+}$  pair share the same energy range:  $[{}^2F_{7/2}, {}^2F_{5/2}5de_g]$  and  $[{}^2F_{5/2}, {}^2F_{7/2}5de_g]$ ; these two manifolds have their  $4f^{13}$  inner-shell of  $Yb^{2+}$  and  $4f^{13}$  shell of  $Yb^{3+}$ , respectively, excited into the  ${}^2F_{5/2}$  spin-orbit multiplet. As a result, all of these energy levels lie close in energy (cf. Table II) and non-radiative relaxation should not be hindered by energy gaps and it should be fast until the luminescent level  $[1\Gamma_{7u}, 2A_{1u}]$  is reached. This step would be reduced to a minimum when the  $[2\Gamma_{7u}, 1E_u]$  level is directly excited.

### 5. Step V. IVCT luminescence.

Step V is the IVCT luminescence  $[1\Gamma_{7u}, 2A_{1u}] \rightarrow [1A_{1g}, {}^2F_{7/2}]$ .

In the last step, the IVCT luminescence consists of three vertical  $Yb^{3+}-Yb^{2+} \rightarrow Yb^{2+}-Yb^{3+}$  intervalence charge transfer transitions. They occur from the excited  $Yb^{3+}({}^2F_{7/2})-Yb^{2+}({}^2F_{5/2}5de_g)$  state  $[1\Gamma_{7u}, 2A_{1u}]$  to the three components of the  $Yb^{2+}(4f^{14})-Yb^{3+}({}^2F_{7/2})$  ground state:  $[1A_{1g}, 1\Gamma_{8u}]$  at  $19974 \text{ cm}^{-1}$ ,  $[1A_{1g}, 1\Gamma_{6u}]$  at  $19999 \text{ cm}^{-1}$ , and  $[1A_{1g}, 1\Gamma_{7u}]$  at  $20508 \text{ cm}^{-1}$ . These leads basically to two wide bands  $530 \text{ cm}^{-1}$  apart.

The vertical transitions occur at the equilibrium structure of the initial  $[1\Gamma_{7u}, 2A_{1u}]$  state:  $(d_L, d_R)_{e, \text{initial}} = (2.201 \text{ \AA}, 2.314 \text{ \AA})$ . This means that the  $Yb^{2+}-Yb^{3+}$  pair that results from the vertical electron transfer is very much stressed, far away from its own equilibrium structure at  $(d_L, d_R)_{e, \text{final}} = (2.330 \text{ \AA}, 2.201 \text{ \AA})$ , which defines the offsets on the left and right moieties of the pair as  $\Delta d_L = +0.129 \text{ \AA}$  and  $\Delta d_R = -0.113 \text{ \AA}$ , and the offset in the normalized concerted vibrational electron transfer reaction coordinate (the distance between  $(d_L, d_R)_{e, \text{initial}}$  and  $(d_L, d_R)_{e, \text{final}}$  in the  $d_L, d_R$  plane) as  $|\Delta Q_{et}| = \sqrt{8} \sqrt{(\Delta d_L)^2 + (\Delta d_R)^2} = 0.49 \text{ \AA}$ . This large offset results in very broad emission bands with full width at half maximum (FWHM) about  $5800 \text{ cm}^{-1}$ , much broader than it could be expected from the regular  ${}^2F_{7/2}5de_g \rightarrow 4f^{14}$  emission, should the latter occur. This is illustrated in Fig. 5, where the simulation of the IVCTL band has been produced for the three electronic origins  $[1\Gamma_{7u}, 2A_{1u}] \rightarrow [1A_{1g}, 1\Gamma_{8u, 6u, 7u}]$  using the semiclassical time-dependent approach of Heller<sup>61-63</sup> with an arbitrary value for the oscillator strengths.

The first reports on the luminescence of  $\text{CaF}_2:\text{Yb}^{2+}$  crystals below 200 K describe a broad structureless band in the yellow-green region formed by two overlapping bands peaking at 17600 and 18200  $\text{cm}^{-1}$ ,<sup>6,8,11</sup> which suggests that the results of the calculations lead to overestimations of the IVCT luminescence by some 2000  $\text{cm}^{-1}$ . Values of the FWHM between 3000 and 4000  $\text{cm}^{-1}$  have been found experimentally, depending on temperature.<sup>11</sup> The 2000  $\text{cm}^{-1}$  overestimation of the calculated peaks of the IVCT bands, together with the 1700  $\text{cm}^{-1}$  underestimation obtained for the calculated  $\text{Yb}^{2+} 4f^{14}-1A_{1g} \rightarrow 4f^{13}5de_g-1T_{1u}$  transition contribute to a smaller calculated red shift of the IVCT luminescence relative to the  $\text{Yb}^{2+}$  excitation than observed: it is found to be about 5600  $\text{cm}^{-1}$  whereas the experimentally measured red shift is about 10000  $\text{cm}^{-1}$ .<sup>11,60</sup>

An important characteristic of the level responsible for the IVCT luminescence,  $[2A_{1u}, 1\Gamma_{7u}]$  (or equivalently  $[1\Gamma_{7u}, 2A_{1u}]$ ), is its very low radiative rate compared with that of upper lying levels. This characteristic is basic for the efficiency of transient photoluminescence enhancement experiments like the ones described next.

### C. Transient IVCT photoluminescence enhancement

Two-frequency transient photoluminescence enhancement measurements on  $\text{CaF}_2:\text{Yb}^{2+}$  single crystals at 10 K have been conducted to probe the energy levels lying above the state responsible for the so far called anomalous emission.<sup>13</sup> The experiments are based on the "radically" different radiative decay rates of the lowest emitting state and higher excited states. The sample, excited in the UV at 365 nm (27400  $\text{cm}^{-1}$ ), is irradiated by an IR pulse. The IR excitation induces significant enhancement of the emission because it populates excited states that have significantly higher radiative rates.<sup>13</sup> So, whereas the radiative rate of the lowest emitting level is in the order of 10<sup>1</sup>ms, the decay of the transient signal is much faster than  $2 \times 10^2 \mu\text{s}$ .<sup>13</sup> Here we show that these experiments can be interpreted as transient IVCT photoluminescence enhancement experiments.

Even though within the diabatic approximation used here we cannot calculate transition moments between pair states and, hence, radiative rates or emission lifetimes, the analyses of the wavefunctions of the parent  $\text{Yb}^{2+}$  and  $\text{Yb}^{3+}$  states can give relevant information on this subject. In this line, the IVCT luminescence can be described as:  $\text{Yb}^{2+} {}^2F_{5/2}5de_g - 2A_{1u} + \text{Yb}^{3+} {}^2F_{7/2}-1\Gamma_{7u} \rightarrow \text{Yb}^{3+} {}^2F_{7/2}-1\Gamma_{7u} + \text{Yb}^{2+} 4f^{14} - 1A_{1g}$ . This indicates that the transition is a double orbital (or spinor) deexcitation, because  $\text{Yb}^{2+}$  gets its  $4f^{13}$  subshell deexcited ( $\text{Yb}^{2+} 4f_{7/2} \rightarrow \text{Yb}^{2+} 4f_{5/2}$ ) at the same time that its  $5de_g$  electron is transferred to fill the  $\text{Yb}^{3+}$  hole ( $\text{Yb}^{2+} 5de_g \rightarrow \text{Yb}^{3+} 4f_{7/2}$ ). This is graphically represented in the scheme labeled double in Fig. 6. Analogous analysis of the emission from the next upper lying level  $[1E_u, 2\Gamma_{7u}]$  yields the conclusion that its IVCT emission  $\text{Yb}^{2+}-\text{Yb}^{3+} [1E_u, 2\Gamma_{7u}] \rightarrow \text{Yb}^{3+}-\text{Yb}^{2+} [2\Gamma_{7u}, 1A_{1g}]$  is a single electron

transfer  $\text{Yb}^{2+} 5de_g \rightarrow \text{Yb}^{3+} 4f_{7/2}$  (see scheme labeled single in Fig. 6). Altogether, it is possible to conclude that the radiative rate of the lowest emission should be much lower than that of the next higher emission, which is in agreement with the lowest emitting state having a long lifetime.<sup>6,8,11,13</sup>

Now, let us discuss the transient photoluminescence enhancement in more detail. Analyses of the transient signals vs. IR wavelength allowed to extract the IR excited state absorption (ESA) spectrum originating in the lowest luminescent level; it consists of two low-intensity sharp peaks at 250 and 1145  $\text{cm}^{-1}$  and a higher intensity broad band from 650 to 950  $\text{cm}^{-1}$ .<sup>13</sup> Other signals found were assigned to trap liberation processes and atmospheric absorptions of the IR free electron laser FEL.<sup>13</sup> The calculated vertical IR ESA spectrum originating in the  $\text{Yb}^{2+}-\text{Yb}^{3+} [2A_{1u}, 1\Gamma_{7u}]$  pair state has been included in Table II. The simulation of the ESA spectrum of Fig. 7, graph (a), has been produced as the superposition of narrow gaussians centered at the energy levels lying below 1700  $\text{cm}^{-1}$ , using equal values of the oscillator strength for each electronic transition. It also consists of three groups of bands which correlate satisfactorily with the experimental values from Ref. 13, which have also been included in Table II and Fig. 7 for comparisons. As in the previous paragraph, analyses of the pair wavefunctions involved in the calculated IR ESA spectrum in terms of the  $\text{Yb}^{2+}$  and  $\text{Yb}^{3+}$  parent states are useful to interpret the IR ESA signals observed, as follows: The sharp experimental peak at 250  $\text{cm}^{-1}$  corresponds to an energy transfer from the  $4f^{13}$  subshell of  $\text{Yb}^{2+}$  to the  $4f^{13}$  shell of  $\text{Yb}^{3+}$ :

$$\text{Yb}^{2+} 4f^{13} [4f_{7/2} \rightarrow 4f_{5/2}] 5de_g + \text{Yb}^{3+} 4f^{13} [4f_{5/2} \rightarrow 4f_{7/2}],$$

or  $[{}^2F_{5/2}5de_g, {}^2F_{7/2}] \rightarrow [{}^2F_{7/2}5de_g, {}^2F_{5/2}]$  within the pair  $\text{Yb}^{2+}-\text{Yb}^{3+}$ , which is a  $4f-4f$  emission in  $\text{Yb}^{2+}$  and a  $4f-4f$  absorption in  $\text{Yb}^{3+}$ . In particular, the two IR ESA bands calculated at 270 and 307  $\text{cm}^{-1}$  correspond to  $[2A_{1u}, 1\Gamma_{7u}] \rightarrow [1E_u, 2\Gamma_{7u}]$  and  $[2A_{1u}, 1\Gamma_{7u}] \rightarrow [1T_{2u}, 2\Gamma_{7u}]$ . The sharp experimental peak at 1145  $\text{cm}^{-1}$  corresponds to the  $2A_{1u} \rightarrow 5T_{1u}$  intraconfigurational absorption occurring in the  $\text{Yb}^{2+}$  center of the pair

$$\text{Yb}^{2+} {}^2F_{5/2}5de_g \rightarrow \text{Yb}^{2+} {}^2F_{5/2}5de_g,$$

as it correlates well with the  $[2A_{1u}, 1\Gamma_{7u}] \rightarrow [5T_{1u}, 1\Gamma_{7u}]$  band calculated at 1069  $\text{cm}^{-1}$ . Finally, the broad band observed from 650 to 950  $\text{cm}^{-1}$  is found to correspond to a set of transitions calculated from 686 to 739  $\text{cm}^{-1}$ , which span a narrower energy interval. Here, higher components of the energy transfer transitions from the  $4f^{13}$  subshell of  $\text{Yb}^{2+}$  to the  $4f^{13}$  shell of  $\text{Yb}^{3+}$ , like those of the lowest IR ESA band, are found together with a third type of excitations which are intraconfigurational  $4f-4f$  transitions between the Stark components of the  $\text{Yb}^{3+}$  moiety:

$$\text{Yb}^{3+} 4f_{7/2} \rightarrow \text{Yb}^{3+} 4f_{7/2}.$$

In all cases, the electronic transitions involve negligible structural reorganization, which explains why they are very narrow bands.

#### D. Excitation of the IR $\text{Yb}^{3+}$ luminescence

A study of the optical properties of  $\text{Yb}^{3+}$ -doped  $\text{CaF}_2$  crystals after application of reducing methods such as  $\gamma$ -irradiation and annealing in hydrogen, was conducted in order to investigate the  $\text{Yb}^{3+}/\text{Yb}^{2+}$  conversion in the  $\text{CaF}_2$  host.<sup>12</sup> The study showed the appearance of the  $4f^{14} \rightarrow 4f^{13}5d$  absorption bands characteristic of  $\text{Yb}^{2+}$ -doped  $\text{CaF}_2$  in the UV absorption spectrum of the treated samples.<sup>12</sup> Two weak overlapping emission bands were observed at room temperature at 565 and 540 nm (17699 and 18519  $\text{cm}^{-1}$ ) in  $\gamma$ -irradiated  $\text{CaF}_2:30\text{at.}\% \text{Yb}^{3+}$  samples excited with 357 nm (28011  $\text{cm}^{-1}$ ), which were identified as the yellow-green anomalous emission of  $\text{Yb}^{2+}$ -doped  $\text{CaF}_2$ , which was observable even at room temperature in this case. A reduction on the intensity of the EPR signals associated with  $\text{Yb}^{3+}$  centers was observed after  $\gamma$ -irradiation at temperatures ranging 10 to 100 K. All of these features were taken as evidences of partial reduction of  $\text{Yb}^{3+}$  to  $\text{Yb}^{2+}$  in the  $\text{CaF}_2$  host.<sup>12</sup>

Since the existence of  $\text{Yb}^{2+}-\text{Yb}^{3+}$  mixed valence pairs in these samples appears to be a reasonable hypothesis, the interpretation of the spectral features mentioned can be done in terms of the IVCT diagrams calculated in this work as explained in the previous sections, where the first absorption of  $\text{Yb}^{2+}$  and the IVCT luminescence mechanism have been described in detail. Yet, the type of samples used in Ref. 12 brings the opportunity to examine the quality of some of the approximations assumed in the IVCT theoretical model used in this paper. In effect, it is worth noticing that departure from cubic site symmetry is far more likely in as-grown  $\text{CaF}_2:\text{Yb}^{3+}$  than in  $\text{CaF}_2:\text{Yb}^{2+}$  crystals due to necessary charge compensation in the former.<sup>64</sup> [Associated with charge compensations, optical absorption signals between 10257 and 10995  $\text{cm}^{-1}$  have been found in  $\text{CaF}_2:\text{Yb}^{3+}$  crystals (this work, cubic: 10763, 11196  $\text{cm}^{-1}$ ) and have been associated with cubic, tetragonal, trigonal, and rhombic sites;<sup>64</sup> they all correspond to different splittings of the  $^2F_{5/2}$  excited multiplet.] This is also true after the  $\text{CaF}_2:\text{Yb}^{3+}$  samples are subjected to reducing treatments.<sup>12</sup> Yet, the shape, number of bands, and peak positions of the IVCT luminescence bands (so far anomalous bands) reported for  $\text{CaF}_2:\text{Yb}^{3+}$  reduced samples in Ref. 12 and for  $\text{CaF}_2:\text{Yb}^{2+}$  crystals in Ref. 6,7, are basically identical: two broad, structureless overlapping bands are observed peaking at 17699 and 18519  $\text{cm}^{-1}$ , and at 17600 and 18200  $\text{cm}^{-1}$ , respectively. This fact suggests that the diabatic approximation proposed here and the disregard of non-cubic splittings due to local charge compensation and/or mutual interaction between the moieties of the  $\text{Yb}^{2+}-\text{Yb}^{3+}$  pairs are reasonable theoretical bases and allow for the quantitative interpretation of the main spectral features of the  $\text{Yb}^{2+}-\text{Yb}^{3+}$  mixed valence pairs at the cost of independent embedded cluster calculations.

In the reduced samples of Ref. 12, the  $4f^{14} \rightarrow 4f^{13}5d$  absorption bands of  $\text{Yb}^{2+}$  were found in the excitation spectrum where the 980 nm (10204  $\text{cm}^{-1}$ ) IR emission of  $\text{Yb}^{3+}$  was monitored. The IVCT energy diagram (Fig. 4) pro-

vides a mechanism for the excitation of the  $\text{Yb}^{3+}$  emission by the first absorption band of  $\text{Yb}^{2+}$ : a generalization of step I, followed by steps II and III<sub>em</sub>. E.g. the lowest  $\text{Yb}^{2+} 4f^{14} \rightarrow ^2F_{7/2}5de_g$  excitation  $A_{1g} \rightarrow 1T_{1u}$  is step I, and the next  $A_{1g} \rightarrow 2 - 4T_{1u}$  excitations will be followed by nonradiative decays to  $1T_{1u}$ ; the lowest  $\text{Yb}^{2+} 4f^{14} \rightarrow ^2F_{5/2}5de_g$  excitation  $A_{1g} \rightarrow 5T_{1u}$  (second  $4f \rightarrow 5d$  band) will be followed by IVCT non-radiative decay [ $^2F_{5/2}5de_g, 1\Gamma_{7u}$ ]  $\rightarrow$  [ $1\Gamma_{7u}, ^2F_{7/2}5de_g$ ], followed by steps II and III<sub>em</sub>; and similar arguments hold for the higher energy states. Obviously, the  $\text{Yb}^{3+}$  emission, step III<sub>em</sub>, competes with step III, which excites the IVCT luminescence through a second photon absorption. However, its quenching ability is probably small given that step III<sub>em</sub> is basically (within the independent embedded cluster approximation) an  $\text{Yb}^{3+} 4f-4f$  electric dipole forbidden transition whereas step III is an electric dipole  $\text{Yb}^{2+} 4f-5d$  allowed absorption.

#### IV. INTERPLAY BETWEEN IVCT AND $5d \rightarrow 4f$ EMISSIONS IN $\text{CaF}_2$ , $\text{SrF}_2$ , $\text{BaF}_2$ , AND $\text{SrCl}_2$ .

As we have discussed, only the very broad yellow-green IVCT luminescence has been detected in  $\text{CaF}_2:\text{Yb}^{2+}$ .<sup>6,8,11</sup> In  $\text{SrF}_2:\text{Yb}^{2+}$ , the equivalent “anomalous” emission has been detected in the red,<sup>8,9</sup> but a second much narrower, blue emission band was also found experimentally and was interpreted as a regular  $5d-4f$  emission from the metastable states  $1E_u$  and  $1T_{2u}$  of  $\text{Yb}^{2+}$ .<sup>10</sup> And in  $\text{BaF}_2:\text{Yb}^{2+}$  there is no emission at all up to 1.5  $\mu\text{m}$  after strong laser excitation in the  $4f-5d$  band.<sup>11</sup> The remaining luminescence combination, i.e. that only regular  $5d-4f$  emission is observed, is found in  $\text{SrCl}_2:\text{Yb}^{2+}$ .<sup>15,16</sup> The  $5d-4f$  emissions of  $\text{SrF}_2:\text{Yb}^{2+}$  and  $\text{SrCl}_2:\text{Yb}^{2+}$  are different: an  $\text{Yb}^{2+}$  electric dipole allowed emission of higher energy, from  $1T_{1u}$ , is present in  $\text{SrCl}_2:\text{Yb}^{2+}$ , which was not found in  $\text{SrF}_2:\text{Yb}^{2+}$  from 4.4 K to room temperature.<sup>10,15,16</sup> In this Section we discussed the reasons for such a chemical dependence of the luminescence. Firstly, we discuss the  $\text{CaF}_2$ ,  $\text{SrF}_2$ ,  $\text{BaF}_2$  chemical series in Sec. IVA. Then, we discuss the  $\text{SrF}_2$ ,  $\text{SrCl}_2$  series in Sec. IVB.

The results of the quantum mechanical calculations of the diabatic potential energy surfaces and the full and selected IVCT energy diagrams for the ground and excited states of the  $\text{Yb}^{2+}-\text{Yb}^{3+}$  embedded pairs in the  $\text{CaF}_2$ ,  $\text{SrF}_2$ ,  $\text{BaF}_2$  hosts are presented in Fig. 6 of Ref. 55 and Fig. 8, and in the  $\text{SrF}_2$ ,  $\text{SrCl}_2$  hosts in Fig. 7 of Ref. 55 and Fig. 9. Vertical transition energies and energy barriers for IVCT reactions between pair states have been included in Tables II and III, respectively (descriptions of their content given in Sec. IIIA are valid and readily adaptable to  $\text{SrF}_2$  and  $\text{BaF}_2$  results). More data can be found in Ref. 55.

##### A. Luminescence of $\text{Yb}^{2+}$ -doped $\text{CaF}_2$ , $\text{SrF}_2$ , and $\text{BaF}_2$

Probably associated with the increasing lattice volume going from  $\text{CaF}_2$  (163.0  $\text{\AA}^3$ , 0%) to  $\text{SrF}_2$  (194.7  $\text{\AA}^3$ , 19%)

to  $\text{BaF}_2$  ( $238.3 \text{ \AA}^3$ , 46%), the offset between the Yb–F equilibrium distance of the ground states of the donor  $\text{Yb}^{2+}$  and acceptor  $\text{Yb}^{3+}$  independent active centers ( $1A_{1g}$  and  $1\Gamma_{7u}$ , respectively), increases significantly from  $0.129 \text{ \AA}$  (0%) to  $0.154 \text{ \AA}$  (19%), to  $0.200 \text{ \AA}$  (55%), in absolute values.<sup>55</sup> Other properties change as well (breathing mode vibrational frequencies, ligand field effects, etc.), but their variations in the series are noticeably smaller.<sup>55</sup> The bond length offsets mentioned determine the values of the normal electron transfer reaction coordinate ( $Q_{et}$ ) at the minimum of the  $\text{Yb}^{2+}-\text{Yb}^{3+}$  pair ground state [ $1A_{1g}, 1\Gamma_{7u}$ ] and, therefore, the offsets between the two equivalent minima  $\text{Yb}^{2+}-\text{Yb}^{3+}$  [ $1A_{1g}, 1\Gamma_{7u}$ ] and  $\text{Yb}^{3+}-\text{Yb}^{2+}$  [ $1\Gamma_{7u}, 1A_{1g}$ ] along the  $Q_{et}$  axis. In the fluoride series this offset increases as:  $|\Delta Q_{et}| = 0.517 \text{ \AA}$  (0%,  $\text{CaF}_2$ ),  $0.616 \text{ \AA}$  (+19%,  $\text{SrF}_2$ ),  $0.802 \text{ \AA}$  (+55%,  $\text{BaF}_2$ ), as it can be observed in Fig. 6 of Ref. 55 and Fig. 8. The different luminescent behaviour of Yb in the fluoride series stems from this trend because, the increase in the offset between the two minima in the IVCT configuration coordinate diagram provokes a shift of the crossing points between the lowest  $\text{Yb}^{2+}-\text{Yb}^{3+}$  [ ${}^2F_{7/2}, 5de_g, {}^2F_{7/2}$ ] states and the stressed branches of the  $\text{Yb}^{3+}-\text{Yb}^{2+}$  IVCT states [ ${}^2F_{7/2}, 4f^{14}$ ] and [ ${}^2F_{5/2}, 4f^{14}$ ], which act as two different non-radiative decay pathways after the first photon excitation: the first decay yields to the pair ground state, and so, to luminescence quenching; the second, leaves  $\text{Yb}^{3+}$  in its  ${}^2F_{5/2}$  excited spin-orbit multiplet, which can ultimately lead to IVCT luminescence. We will see here how the magnitude of the energy barriers for these crossings are responsible for either luminescence quenching, as in  $\text{BaF}_2$ , or interplay between regular  $5d-4f$  and IVCT luminescence, as in the  $\text{CaF}_2$  and  $\text{SrF}_2$  cases. This is summarized in Fig. 10.

### 1. Luminescence quenching in $\text{BaF}_2:\text{Yb}^{2+}$

The crossing between  $\text{Yb}^{2+}-\text{Yb}^{3+}$  [ ${}^2F_{7/2}, 5de_g, {}^2F_{7/2}$ ] and  $\text{Yb}^{3+}-\text{Yb}^{2+}$  [ ${}^2F_{7/2}, 4f^{14}$ ] that enables quenching of the luminescence (step  $\text{II}_{\text{qch}}$ ) by direct non-radiative decay to the ground state after the first photon absorption (step I), i.e. from  $\text{Yb}^{2+}-\text{Yb}^{3+}$  [ $1E_u, 1\Gamma_{7u}$ ] to  $\text{Yb}^{3+}-\text{Yb}^{2+}$  [ $1\Gamma_{7u}, 1A_{1g}$ ], varies very strongly in the fluoride series (cf. Table III and Fig. 8):  $1680 \text{ cm}^{-1}$  ( $\text{CaF}_2$ ),  $818 \text{ cm}^{-1}$  ( $\text{SrF}_2$ ),  $261 \text{ cm}^{-1}$  in  $\text{BaF}_2$ . This result suggests that step  $\text{II}_{\text{qch}}$  should result in appreciable quenching of the luminescence in  $\text{BaF}_2$  after  $4f-5d$  excitation. This observation holds both for IVCT and  $5d-4f$  luminescence and it is in line with experimental evidences.<sup>11</sup> Then, we can say that  $\text{BaF}_2:\text{Yb}^{2+}-\text{Yb}^{3+}$  belongs to the case *D* depicted in Fig. 10.

### 2. Interplay between IVCT and $5d-4f$ emissions in $\text{CaF}_2$ and $\text{SrF}_2$

The second important non-radiative pathway following excitation is step II (see Sec. III B), which enables IVCT non-radiative decay to the  $\text{Yb}^{3+}-\text{Yb}^{2+}$  [ $2\Gamma_{7u}, 1A_{1g}$ ] excited state

and is part of the IVCT luminescence mechanism. The shifts of the energy barriers leading to step II from  $\text{CaF}_2$  to  $\text{SrF}_2$  allow to interpret the different luminescent behaviour in these two hosts, as discussed next.

The energy barrier of IVCT crossing from  $\text{Yb}^{2+}-\text{Yb}^{3+}$  [ $1E_u, 1\Gamma_{7u}$ ] to  $\text{Yb}^{3+}-\text{Yb}^{2+}$  [ $2\Gamma_{7u}, 1A_{1g}$ ] increases from  $\text{CaF}_2$  to  $\text{SrF}_2$ :  $14 \text{ cm}^{-1}$  ( $\text{CaF}_2$ ),  $148 \text{ cm}^{-1}$  ( $\text{SrF}_2$ ). This suggests that [ $1E_u, 1\Gamma_{7u}$ ] is more stable in  $\text{SrF}_2$  than in  $\text{CaF}_2$ . So, regular  $\text{Yb}^{2+}$   $5d-4f$  emission from this level should be more likely in  $\text{SrF}_2$ , where, as a matter of fact, it has been observed.<sup>10</sup> For the same reason, its contribution to exciting the IVCT luminescence through steps II to IV is much less likely in  $\text{SrF}_2$  than in  $\text{CaF}_2$ , which correlates well with the significantly overall smaller emission lifetime of the IVCT (anomalous) luminescence measured in  $\text{SrF}_2$  compared with  $\text{CaF}_2$ .<sup>11</sup> Then, we can say that  $\text{SrF}_2:\text{Yb}^{2+}$  and  $\text{CaF}_2:\text{Yb}^{2+}$  belong, respectively, to a case intermediate between *C* and *B*, and to case *B* depicted in Fig. 10.

In contrast, the energy barriers for crossing from [ $1T_{1u}, 1\Gamma_{7u}$ ] to [ $2\Gamma_{7u}, 1A_{1g}$ ]:  $49 \text{ cm}^{-1}$  ( $\text{CaF}_2$ ) and  $10 \text{ cm}^{-1}$  ( $\text{SrF}_2$ ), are comparable (although slightly smaller in the latter), which suggests that [ $1T_{1u}, 1\Gamma_{7u}$ ] should contribute significantly to the excitation of the IVCT luminescence in both hosts, especially at very low temperatures, since non-radiative multiphonon decay from this level to the [ $1E_u, 1\Gamma_{7u}$ ] should gradually quench this contribution in favour of a build up of the population of [ $1E_u, 1\Gamma_{7u}$ ] on a temperature dependent basis.<sup>16,59</sup> Whereas this temperature dependent build up implies further excitation of the IVCT luminescence in  $\text{CaF}_2:\text{Yb}^{2+}$  (because [ $1E_u, 1\Gamma_{7u}$ ] preferentially undergoes step II of the IVCT luminescence), it contributes to increasing the intensity of the  $\text{Yb}^{2+}$   $5d-4f$  blue emission [ $1E_u, 1\Gamma_{7u}$ ]  $\rightarrow$  [ $1A_{1g}, 1\Gamma_{7u}$ ] in  $\text{SrF}_2:\text{Yb}^{2+}$  (because  $5d-4f$  emission is the preferred pathway for [ $1E_u, 1\Gamma_{7u}$ ] depopulation in this material). Altogether, these results allow to explain the different variation of the IVCT luminescence intensity with temperature in  $\text{SrF}_2$  compared with  $\text{CaF}_2$ : IVCT luminescence intensity reaches its maximum very sharply in  $\text{SrF}_2:\text{Yb}^{2+}$ , at very low temperature: 20 K, and quenches already at 140 K; maximum intensity is reached more gradually at 110 K in  $\text{CaF}_2$  and quenching is observed at 180 K (Ref. 11) (this quenching has been connected with branching to the ground state in Sec. III B). Correspondingly, the intensity of the  $5d-4f$  emission [ $1E_u, 1\Gamma_{7u}$ ]  $\rightarrow$  [ $1A_{1g}, 1\Gamma_{7u}$ ] in  $\text{SrF}_2$  upon excitation in the [ $1T_{1u}, 1\Gamma_{7u}$ ] state (355 nm) is shown to be significantly higher than that measured upon direct excitation in the [ $1E_u, 1\Gamma_{7u}$ ] state (370 nm) beyond 140 K, which further reveals the temperature dependent [ $1T_{1u}, 1\Gamma_{7u}$ ]  $\rightarrow$  [ $1E_u, 1\Gamma_{7u}$ ] build up at the expense of the [ $1T_{1u}, 1\Gamma_{7u}$ ]  $\rightarrow$  [ $2\Gamma_{7u}, 1A_{1g}$ ] decay and IVCT luminescence.

Beyond step II, which has been discussed so far, the mechanism for IVCT luminescence in  $\text{SrF}_2$  is the same as in  $\text{CaF}_2$  and leads to a very broad band consisting of two overlapping bands corresponding to the three  $\text{Yb}^{3+}-\text{Yb}^{3+}$  [ $1\Gamma_{7u}, 2A_{1u}$ ]  $\rightarrow$   $\text{Yb}^{2+}-\text{Yb}^{3+}$  [ $4f^{14}, {}^2F_{7/2}$ ] vertical transitions at 17698, 17716, and 18121  $\text{cm}^{-1}$ . Its FWHM is about 6000  $\text{cm}^{-1}$  as it can be seen in Fig. 5. The peak en-

ergy and FWHM found experimentally are  $12670\text{ cm}^{-1}$  and  $4800\text{ cm}^{-1}$ . This indicates that the underestimation of the peak energy found in  $\text{CaF}_2$  becomes larger in the  $\text{SrF}_2$  host. In  $\text{SrF}_2$ , the agreement between the calculated IR ESA spectrum and the one deduced from transient photoluminescence enhancement experiments in Ref. 14 is comparable to that in  $\text{CaF}_2$ . Both the theoretical and experimental spectra can be compared in Table II and Fig. 7. The interpretation of the observed bands is the same as in the  $\text{CaF}_2$  case.

### 3. IVCT absorption in $\text{Yb}^{2+}$ -doped $\text{SrF}_2$

Finally, we would like to report on the IVCT absorption bands which, according to our interpretation, have been detected in the excitation spectra of  $\text{Yb}^{2+}$ -doped  $\text{SrF}_2$  (Ref. 11) even though they have not been identified as such. We are not aware of similar experiments in the other hosts.

We will try to interpret the excitation spectra of the  $\text{SrF}_2:\text{Yb}^{2+}$  blue and red emissions<sup>11</sup> using the calculations presented in this paper. According to them, a large number of close lying states of the  $\text{Yb}^{2+}-\text{Yb}^{3+}$  [ ${}^2F_{7/2}5de_g, {}^2F_{7/2}$ ] configuration lie above its lowest state, [ $1E_u, 1\Gamma_{7u}$ ], forming a dense manifold  $5500\text{ cm}^{-1}$  wide. This can be seen in Fig. 6 of Ref. 55 (first manifold of states plotted with solid blue lines); some of the levels are plotted in Fig. 8 and are tabulated in the absorption spectrum from the [ $1A_{1g}, 1\Gamma_{7u}$ ] ground state in Table II (see also Ref. 55). In the vertical absorption spectrum from the [ $1A_{1g}, 1\Gamma_{7u}$ ] ground state (Table II), this manifold is crossed by the stressed IVCT [ ${}^2F_{5/2}, 4f^{14}$ ] branches of  $\text{Yb}^{3+}-\text{Yb}^{2+}$  [ $2\Gamma_{7u}, 1A_{1g}$ ] and [ $2\Gamma_{8u}, 1A_{1g}$ ] (dashed red lines in Fig. 6 of Ref. 55 and in Fig. 8) which are found at  $28545$  and  $28809\text{ cm}^{-1}$  ( $4070$  and  $4333\text{ cm}^{-1}$  above the [ $1E_u, 1\Gamma_{7u}$ ] state).

Then, according to the mechanism discussed in Sec. III B, IVCT luminescence will be excited if these branches are reached either by crossings (like above) or by direct vertical IVCT absorptions from the ground state (like here, in the excitation spectrum). This explains the differences observed in the experimental excitation spectra: The excitation spectra of the IVCT luminescence consists of one intense and very broad band peaking at about  $351\text{ nm}$  ( $28400\text{ cm}^{-1}$ ) as one can read in Fig. 3 of Ref. 11. This band can be assigned to the vertical IVCT absorptions  $\text{Yb}^{2+}-\text{Yb}^{3+}$  [ $1A_{1g}, 1\Gamma_{7u}$ ]  $\rightarrow$   $\text{Yb}^{3+}-\text{Yb}^{2+}$  [ $2\Gamma_{7u}, 1A_{1g}$ ], [ $2\Gamma_{8u}, 1A_{1g}$ ]. The band is broad due to the large offset between the to minima [ $1A_{1g}, 1\Gamma_{7u}$ ] and [ $2\Gamma_{7u}, 1A_{1g}$ ] along the  $Q_{et}$  axis ( $0.616\text{ \AA}$ ). Interestingly, the broad band shows a shoulder in its high energy side, which indicates that non-radiative decay to the IVCT [ $2\Gamma_{7u}, 1A_{1g}$ ] branch from states lying above (like the electric dipole allowed [ $4T_{1u}, 1\Gamma_{7u}$ ]) could also excite the IVCT luminescence with sufficient efficiency so as to be observed as a shoulder from the main IVCT absorption excitation channel. Correspondingly, the excitation spectrum of the blue [ $1E_u, 1\Gamma_{7u}$ ]  $\rightarrow$  [ $1A_{1g}, 1\Gamma_{7u}$ ] emission shows the electronic structure of the [ ${}^2F_{7/2}5de_g, {}^2F_{7/2}$ ] manifold inter-

rupted by a dip, which coincides with the maximum of the intense IVCT absorption band of the IVCT luminescence excitation spectrum. Also, the shoulder of the latter and the fourth and highest intense peak of the former lie very close, which suggests the presence of the electric dipole allowed [ $1A_{1g}, 1\Gamma_{7u}$ ]  $\rightarrow$  [ $4T_{1u}, 1\Gamma_{7u}$ ] transition. It is interesting to note that in most of the experiments reported for  $\text{SrF}_2:\text{Yb}^{2+}$  a larger wavelength (typically,  $355\text{ nm}$ ) has been used to study the luminescent behaviour of the anomalous emission.

The IVCT absorption band we have just assigned can be interpreted as the following one electron transfer:  $\text{Yb}^{2+} 4f_{5/2} \rightarrow \text{Yb}^{3+} 4f_{7/2}$ . It differs from the commonly observed IVCT absorptions in mixed valence compounds in that the final state of the pair upon electron transfer is not the stressed ground state, but, rather, a stressed excited state. In this case, the  $\text{Yb}^{3+}$  part of the pair after electron transfer appears to be in the  $4f^{13}({}^2F_{5/2})$  excited multiplet. This  $4f-4f$  electron transfer is probably weaker than the close lying  $4f \rightarrow 5d$  transitions in the absorption spectrum; however, it is more efficient in exciting the IVCT luminescence, because of its direct decay (step II) not facing an energy barrier, which explains its relative intensity in the excitation spectrum.

### B. Interplay between IVCT and $5d-4f$ emissions in $\text{SrF}_2$ and $\text{SrCl}_2$

The dual character of the luminescence of Yb in  $\text{SrF}_2$  we have just discussed, disappears in the  $\text{SrCl}_2$  host, where the IVCT luminescence is not observed: only regular  $5d-4f$  emission bands have been assigned in this case. However, the emission spectrum of  $\text{SrCl}_2:\text{Yb}^{2+}$  is very complex. This complexity stems precisely from the fact that the IVCT luminescence mechanism cannot occur, hence,  $5d-4f$  bands which are not observable in  $\text{SrF}_2:\text{Yb}^{2+}$ , become uncovered in  $\text{SrCl}_2:\text{Yb}^{2+}$ . The purpose of this section is to explain why this is so even if the existence of  $\text{Yb}^{2+}-\text{Yb}^{3+}$  mixed valence pairs is likely.<sup>16,22,23</sup> We do not intend to discuss the complex  $4f-5d$  spectroscopy of  $\text{SrCl}_2:\text{Yb}^{2+}$ , which has been the subject of a number of experimental and theoretical studies.<sup>15,16,57,65,66</sup>

In the host series  $\text{SrF}_2, \text{SrCl}_2$ , it is the chemical change what leads the variations of the local properties of the  $\text{Yb}^{2+}$  and  $\text{Yb}^{3+}$  moieties of the  $\text{Yb}^{2+}-\text{Yb}^{3+}$  pairs, rather than the structural change. In particular, the energies of the breathing mode of the donor ( $\text{YbX}_8$ )<sup>6-</sup> and acceptor ( $\text{YbX}_8$ )<sup>5-</sup> embedded clusters clearly show the chemical change, so that the mean values of the ground state vibrational frequencies  $\bar{\omega}_{a_{1g}} = [\omega_{a_{1g}}(1A_{1g}) + \omega_{a_{1g}}(1\Gamma_{7u})]/2$ , decrease from  $402\text{ cm}^{-1}$  (0%,  $\text{SrF}_2$ ) to  $246\text{ cm}^{-1}$  (39 %,  $\text{SrCl}_2$ ). These mean values basically determine the curvatures of the diabatic potential energy surfaces and of the IVCT energy diagrams of the  $\text{Yb}^{2+}-\text{Yb}^{3+}$  embedded pairs. The change is very clear in Fig. 7 of Ref. 55 and Fig. 9. As an effect, the crossing points between the lowest  $\text{Yb}^{2+}-\text{Yb}^{3+}$  [ ${}^2F_{7/2}5de_g, {}^2F_{7/2}$ ] states and the stressed

branches of the  $\text{Yb}^{3+}-\text{Yb}^{2+}$  ground and excited configurations [ ${}^2F_{7/2}, 4f^{14}$ ] and [ ${}^2F_{5/2}, 4f^{14}$ ] are drastically shifted in  $\text{SrCl}_2$  (see Fig. 9 and Table III). And as a consequence, none of the two non-radiative pathways is available in  $\text{SrCl}_2$  anymore. We can say that  $\text{SrCl}_2:\text{Yb}^{2+}-\text{Yb}^{3+}$  belongs to the case A in Fig. 10. Therefore, the first conclusion driven from the  $\text{SrCl}_2:\text{Yb}^{2+}-\text{Yb}^{3+}$  IVCT energy diagrams is that the IVCT luminescence observed in  $\text{CaF}_2$  and  $\text{SrF}_2$  cannot occur in this host. The second conclusion is that not only is the [ $1E_u, 1\Gamma_{7u}$ ] state very stable, but also the higher electric dipole allowed [ $1T_{1u}, 1\Gamma_{7u}$ ] state is, since it cannot decay through step II, like in  $\text{CaF}_2$  and  $\text{SrF}_2$ . This means that both states can luminesce in a wide range of temperatures (blue arrows in Fig. 9) and that the temperature dependent multiphonon relaxation from [ $1T_{1u}, 1\Gamma_{7u}$ ] to [ $1E_u, 1\Gamma_{7u}$ ], which influenced the intensities of the blue and red emissions of  $\text{SrF}_2$  discussed above, applies now to the interplay between radiative and non radiative decays from [ $1T_{1u}, 1\Gamma_{7u}$ ], with the additional complexity arising from the Boltzmann population of close lying states above the  $1T_{1u}$  before room temperature is reached. All of which results in a complex, but well understood temperature dependence of the relative intensities and lifetimes of the two emission bands.<sup>16</sup>

In addition to the two emission bands from [ $1T_{1u}, 1\Gamma_{7u}$ ] and [ $1E_u, 1\Gamma_{7u}$ ], observed peaking at 26500 and 24700  $\text{cm}^{-1}$ , respectively (this work: 25500 and 22900  $\text{cm}^{-1}$ ), Witzke *et al.* reported other three emission bands peaking at 19000, 23900, and 25400  $\text{cm}^{-1}$ , which were ruled out as internal transitions of the  $\text{Yb}^{2+}$  ion and were called defect bands involving, possibly,  $\text{Yb}^{3+}$  ions or  $\text{Yb}^{3+}-\text{Yb}^{2+}$  pairs.<sup>15</sup> The band peaking at 19000  $\text{cm}^{-1}$  could be associated with the IVCT luminescence  $\text{Yb}^{2+}-\text{Yb}^{3+}$  [ $1E_u, 1\Gamma_{7u}$ ]  $\rightarrow$   $\text{Yb}^{3+}-\text{Yb}^{2+}$  [ $1\Gamma_{7u}, 1A_{1g}$ ], calculated as a vertical transition at 17200  $\text{cm}^{-1}$  (see green arrows in Fig. 9).

## V. CONCLUSIONS

*Ab initio* quantum mechanical calculations of the electronic structure of  $\text{Yb}^{2+}-\text{Yb}^{3+}$  mixed valence pairs in fluorites allow to conclude the existence of two-photon excited IVCT luminescence in Yb-doped  $\text{CaF}_2$  and  $\text{SrF}_2$ . The IVCT emission is found to be a bielectronic deexcitation involving electron transfer from the donor to the acceptor moieties of the  $\text{Yb}^{2+}-\text{Yb}^{3+}$  pair,  $\text{Yb}^{2+} 5d e_g \rightarrow \text{Yb}^{3+} 4f_{7/2}$ , and a  $4f_{7/2} \rightarrow 4f_{5/2}$  deexcitation within the  $\text{Yb}^{2+} 4f^{13}$  subshell:  $\text{Yb}^{2+}-\text{Yb}^{3+}$  [ ${}^2F_{5/2} 5d e_g, {}^2F_{7/2}$ ]  $\rightarrow$   $\text{Yb}^{3+}-\text{Yb}^{2+}$  [ ${}^2F_{7/2}, 4f^{14}$ ]. Hence, it is a very slow rate radiative process. It is excited by a very efficient two-photon mechanism where each photon provokes the same strong  $4f^{14}-1A_{1g} \rightarrow 4f^{13}({}^2F_{7/2}) 5d e_g-1T_{1u}$  absorption in the  $\text{Yb}^{2+}$  part of the pair: the first one, from the pair ground state; the second one, from an excited state of the pair whose  $\text{Yb}^{3+}$  moiety is in the higher  $4f^{13}({}^2F_{5/2})$  spin-orbit multiplet. The band widths of the emissions are very large, in analogy with the wide band widths of well-known IVCT absorptions of

transition metal mixed valence compounds.

The calculated IVCT energy diagrams show that two important non-radiative decay pathways may occur after the first photon excitation, which involve non-radiative  $\text{Yb}^{2+}-\text{Yb}^{3+} \rightarrow \text{Yb}^{3+}-\text{Yb}^{2+}$  electron transfer (see graphical conclusion Fig. 10). One, leads to the ground state [ $4f^{13}({}^2F_{7/2}), 4f^{14}$ ] and quenches any emission (black line in Fig. 10); the other, leads to the excited state [ $4f^{13}({}^2F_{5/2}), 4f^{14}$ ] from where the (second-photon) IVCT luminescence excitation takes place (red line in Fig. 10). The structural change in the  $\text{CaF}_2$ ,  $\text{SrF}_2$ ,  $\text{BaF}_2$  series and the chemical change in the  $\text{SrF}_2$ ,  $\text{SrCl}_2$  series, influence the topology of the calculated IVCT energy diagrams and shift the crossings with both decay pathways making the quenching decay the most likely in  $\text{BaF}_2$ , the decay towards IVCT luminescence excitation the most likely in  $\text{CaF}_2$  and  $\text{SrF}_2$ , whereas none of the two decays occur in the  $\text{SrCl}_2$  case, all of which leads to total quenching of any emission in  $\text{BaF}_2$  (case D), IVCT luminescence only in  $\text{CaF}_2$  (case B), dual IVCT and  $5d-4f$  emissions in  $\text{SrF}_2$  (intermediate case between B and C), and only  $5d-4f$  emissions in  $\text{SrCl}_2$  (case A), as experimentally observed.

The electronic structure of the  $\text{Yb}^{2+}-\text{Yb}^{3+}$  pairs has been calculated within the diabatic and independent  $\text{Yb}^{2+}$  and  $\text{Yb}^{3+}$  embedded cluster approximations. The donor ( $\text{YbX}_8$ )<sup>6-</sup> and acceptor ( $\text{YbX}_8$ )<sup>5-</sup> *ab initio* wavefunctions and energies have been calculated using high quality, well-established *ab initio* quantum chemical methods, including: extended basis sets, non-dynamic and dynamic electron correlation, relativistic effects up to spin-orbit coupling, and quantum mechanical host embedding, all of them, at the highest levels of methodology compatible with the need to combine them all at once. The two series of hosts chosen to demonstrate the capabilities and limitations of the IVCT model presented span a very complex luminescence scenario for validation. In this context, the overall agreement of the theoretical and experimental results including different types of samples ( $\text{Yb}^{2+}$ -doped,  $\text{Yb}^{3+}$ -doped) and experimental techniques: emission, excitation, photoluminescence enhancement spectra and their variation with temperature, is very satisfactory and allows to draw the conclusion that the anomalous luminescence of  $\text{Yb}^{2+}$  associated so far with impurity-trapped excitons is, rather, an IVCT luminescence associated with  $\text{Yb}^{2+}-\text{Yb}^{3+}$  mixed valence pairs. We also conclude that the broad band observed in the excitation spectrum of the so far called anomalous emission of  $\text{Yb}^{2+}$ -doped  $\text{SrF}_2$  is a broad IVCT absorption band corresponding to the following  $\text{Yb}^{2+} 4f_{5/2} \rightarrow \text{Yb}^{3+} 4f_{7/2}$  electron transfer.

## Acknowledgments

This work was partly supported by a grant from Ministerio de Economía y Competitividad, Spain (Dirección General de Investigación y Gestión del Plan Nacional de I+D+i, MAT2011-24586).

- \* Corresponding author; Electronic address: zoila.barandiaran@uam.es
- 1 C. W. E. van Eijk, *Phys. Med. Biol.* **47**, R85 (2002).
  - 2 G. Liu and B. Jacquier, eds., *Spectroscopic Properties of Rare Earths in Optical Materials* (Springer, Berlin, 2005).
  - 3 C. R. Ronda, ed., *Luminescence: From Theory to Applications* (Wiley-VCH, Weinheim, 2007).
  - 4 M. J. Weber, *J. Lumin.* **100**, 35 (2002).
  - 5 P. Dorenbos, *J. Phys.: Condens. Matter* **15**, 2645 (2003).
  - 6 P. P. Feofilov, *Opt. Spektrosk.* **1**, 992 (1956).
  - 7 A. A. Kaplyanskii and P. P. Feofilov, *Opt. Spectrosc.* **13**, 129 (1962).
  - 8 E. G. Reut, *Opt. Spectrosc.* **40**, 55 (1976).
  - 9 D. S. McClure and C. Pédrini, *Phys. Rev. B* **32**, 8465 (1985).
  - 10 B. Moine, C. Pédrini, D. S. McClure and H. Bill, *J. Lumin.* **40&41**, 299 (1988).
  - 11 B. Moine, B. Courtois and C. Pédrini, *J. Phys. France* **50**, 2105 (1989).
  - 12 S. M. Kaczmarek, T. Tsuboi, M. Ito, G. Boulon, and G. Leniec, *J. Phys.: Condens. Matter* **17**, 3771 (2005).
  - 13 M. F. Reid, P. S. Senanayake, J.-P. R. Wells, G. Berden, A. Meijerink, A. J. Salkeld, C.-K. Duan and R. J. Reeves, *Phys. Rev. B* **84**, 113110 (2011).
  - 14 P. S. Senanayake, J. P. R. Wells, M. F. Reid, G. Berden, A. Meijerink and R. J. Reeves, *J. Lumin.* **133**, 81 (2013).
  - 15 H. Witzke, D. S. McClure, and B. Mitchell, in *Luminescence of Crystals, Molecules, and Solutions*, edited by F. E. Williams (Plenum, New York, 1973), p. 598.
  - 16 Z. Pan, C. Duan, and P. A. Tanner, *Phys. Rev. B* **77**, 085114 (2008).
  - 17 A. Bessière, P. Dorenbos, C. van Eijk, L. Pidol, K. Krämer, and H. Güdel, *J. Phys.: Condens. Matter* **16**, 1887 (2004).
  - 18 A. Bessière, P. Dorenbos, C. van Eijk, K. Krämer, H. Güdel, and A. Galtayries, *J. Lumin.* **117**, 187 (2006).
  - 19 M. Grinberg, *J. Lumin.* **131**, 433 (2011).
  - 20 E. Loh, *Phys. Rev.* **175**, 533 (1968).
  - 21 E. Loh, *Phys. Rev.* **184**, 348 (1969).
  - 22 L. Su, J. Xu, H. Li, L. Wen, W. Yang, Z. Zhao, J. Si, Y. Dong and G. Zhou, *J. Cryst. Growth* **277**, 264 (2005).
  - 23 L. Su, J. Xu, H. Li, L. Wen, Y. Zhu, Z. Zhao, Y. Dong, G. Zhou and J. Si, *Chem. Phys. Lett.* **406**, 254 (2005).
  - 24 L. Seijo and Z. Barandiarán, "Intervalence charge transfer luminescence: The anomalous luminescence of cerium-doped  $\text{Cs}_2\text{LiLuCl}_6$  elpasolite," *J. Chem. Phys.*, accepted.
  - 25 J. W. Verhoeven, *Pure Appl. Chem.* **68**, 2223 (1996).
  - 26 R. A. Marcus, *Annu. Rev. Phys. Chem.* **15**, 155 (1964).
  - 27 G. C. Allen and N. S. Hush, *Prog. Inorg. Chem.* **8**, 357 (1967).
  - 28 N. S. Hush, *Prog. Inorg. Chem.* **8**, 391 (1967).
  - 29 M. Robin and P. Day, *Adv. Inorg. Chem. Radiochem.* **10**, 247 (1968).
  - 30 S. B. Piepho, E. R. Krausz, and P. N. Schatz, *J. Amer. Chem. Soc.* **100**, 2996 (1975).
  - 31 G. Blasse, *Struct. Bond.* **76**, 153 (1991).
  - 32 W. van Schaik, S. Lizzo, W. Smit, and G. Blasse, *J. Electrochem. Soc.* **140**, 216 (1993).
  - 33 Z. Barandiarán, A. Meijerink, and L. Seijo, "Intervalence charge transfer and metal-to-metal charge transfer configuraton coordinate diagrams of dopant pairs in solids," in preparation.
  - 34 R. McWeeny, *Proc. R. Soc. Lond. A* **253**, 242 (1959).
  - 35 G. Karlström, R. Lindh, P. A. Malmqvist, B. O. Roos, U. Ryde, V. Varyazov, P. O. Widmark, M. Cossi, B. Schimmelpfennig, P. Neogrady, et al., *Comput. Mater. Sci.* **28**, 222 (2003).
  - 36 R. W. G. Wyckoff, *Crystal Structures*, vol. 1, 2nd. edn. (Interscience Publishers, 1982).
  - 37 M. Douglas and N. M. Kroll, *Ann. Phys. (N.Y.)* **82**, 89 (1974).
  - 38 B. A. Hess, *Phys. Rev. A* **33**, 3742 (1986).
  - 39 B. O. Roos, R. Lindh, P. A. Malmqvist, V. Varyazov, and P. O. Widmark, *J. Phys. Chem. A* **108**, 2851 (2005).
  - 40 B. O. Roos, R. Lindh, P. A. Malmqvist, V. Varyazov, and P. O. Widmark, *J. Chem. Phys.* **112**, 11431 (2008).
  - 41 Z. Barandiarán and L. Seijo, *J. Chem. Phys.* **89**, 5739 (1988).
  - 42 L. Seijo and Z. Barandiarán, in *Computational Chemistry: Reviews of Current Trends*, edited by J. Leszczynski (World Scientific, Singapore, 1999), vol. 4, pp. 55–152.
  - 43 A. Gellé and M.-B. Lepetit, *J. Chem. Phys.* **128**, 244716 (2008).
  - 44 Z. Barandiarán and L. Seijo, *J. Chem. Phys.* **138**, 074102 (2013).
  - 45 J. Olsen, B. O. Roos, P. Jørgensen, and J. A. Jensen, *J. Chem. Phys.* **89**, 2185 (1988).
  - 46 P.-A. Malmqvist, A. Rendell, and B. O. Roos, *J. Phys. Chem.* **94**, 5477 (1990).
  - 47 P.-Å. Malmqvist, K. Pierloot, A. R. Moughal Shahi, C. J. Cramer and L. Gagliardi, *J. Chem. Phys.* **128**, 204109 (2008).
  - 48 A. Zaitsevskii and J.-P. Malrieu, *Chem. Phys. Lett.* **233**, 597 (1995).
  - 49 J. Finley, P.-A. Malmqvist, B. O. Roos, and L. Serrano-Andrés, *Chem. Phys. Lett.* **288**, 299 (1998).
  - 50 G. Ghigo, B. O. Roos, and P.-Å. Malmqvist, *Chem. Phys. Lett.* **396**, 142 (2004).
  - 51 N. Forsberg and P.-A. Malmqvist, *Chem. Phys. Lett.* **274**, 196 (1997).
  - 52 P. A. Malmqvist, B. O. Roos, and B. Schimmelpfennig, *Chem. Phys. Lett.* **357**, 230 (2002).
  - 53 B. A. Hess, C. M. Marian, U. Wahlgren, and O. Gropen, *Chem. Phys. Lett.* **251**, 365 (1996).
  - 54 Detailed core and embedding AIMP data libraries in electronic format are available from the authors upon request or directly at the address <http://www.uam.es/quimica/aimp/Data/AIMPLibs.html>. See also Ref. 35.
  - 55 See supplemental material at [URL] for detailed results of the quantum mechanical calculations on the donor  $(\text{YbX}_8)^{6-}$  and acceptor  $(\text{YbX}_8)^{5-}$  cubic clusters embedded in the four  $\text{CaF}_2$ ,  $\text{SrF}_2$ ,  $\text{BaF}_2$ , and  $\text{SrCl}_2$  fluorite-type hosts. Diabatic IVCT energy diagrams and vertical absorptions and emissions of  $\text{Yb}^{2+}-\text{Yb}^{3+}$  pairs in the same hosts, calculated at the equilibrium geometry of various initial states of the pairs are also included.
  - 56 B. Ordejón, L. Seijo, and Z. Barandiarán, *J. Chem. Phys.* **126**, 194712 (2007).
  - 57 G. Sánchez-Sanz, L. Seijo, and Z. Barandiarán, *J. Chem. Phys.* **133**, 114509 (2010).
  - 58 Z. Barandiarán and L. Seijo, to be published.
  - 59 J. Grimm and H. U. Güdel, *Chem. Phys. Lett.* **404**, 40 (2005).
  - 60 J. Rubio, *J. Phys. Chem. Solids* **52**, 101 (1991).
  - 61 E. J. Heller, *J. Chem. Phys.* **62**, 1544 (1975).
  - 62 E. J. Heller, *Acc. Chem. Res.* **14**, 368 (1981).
  - 63 J. I. Zink and K. S. Shin, in *Advances in Photochemistry* (Wiley, New York, 1991), vol. 16, pp. 119–214.
  - 64 J. Kirton and S. D. McLaughlan, *Phys. Rev.* **155**, 279 (1967).
  - 65 T. S. Piper, J. P. Brown, and D. S. McClure, *J. Chem. Phys.* **46**, 1353 (1967).
  - 66 G. Sánchez-Sanz, L. Seijo, and Z. Barandiarán, *J. Chem. Phys.* **133**, 114506 (2010).

<sup>67</sup> Z. J. Kiss, Phys. Rev. **127**, 3 (1962).

---



TABLE I: Spectroscopic constants and analyses of the spin-orbit wave functions of the electronic states of independent  $\text{Yb}^{2+}$  and  $\text{Yb}^{3+}$  -doped  $\text{CaF}_2$  cubic defects. Yb-F bond distances,  $d_e$ , in Å; totally symmetric vibrational frequencies of the  $\text{YbF}_8$  stretching mode,  $\omega_{a_{1g}}$ , in  $\text{cm}^{-1}$ ; minimum-to-minimum energy differences,  $T_e$ , relative to the ground states, in  $\text{cm}^{-1}$ .  $1A_{1g} \rightarrow iT_{1u}$  absorption oscillator strengths of electric dipole allowed electronic transitions,  $f_i$ , are given relative to that to  $1T_{1u}$ :  $f_i = 2.013 \times 10^{-2}$ . Manifold averages and mean square deviations of the individual values are indicated. Higher lying excited states of  $\text{Yb}^{2+}$  can be found in Ref. 55

State	$d_e$	$\omega_{a_{1g}}$	$T_e$	$f_i/f_1$	weights of terms larger than 10% <sup>a</sup>						
Yb <sup>2+</sup> -doped CaF <sub>2</sub>											
1	$A_{1g}$	2.329	417	0	100.0	$1^1A_{1g}$					
$4f^{13}(^2F_{7/2})5de_g$ submanifold; $\langle d_e \rangle = 2.315 \pm 0.001$ ; $\langle \omega_{a_{1g}} \rangle = 423 \pm 1$											
1	$E_u$	2.317	423	23510	89.21	$1^3T_{1u}$					
1	$T_{2u}$	2.317	423	23548	89.94	$1^3T_{1u}$					
1	$T_{1u}$	2.316	423	25636	1.000	42.33	$1^3T_{1u}$	34.07	$1^1T_{1u}$	19.47	$1^3T_{2u}$
1	$A_{2u}$	2.315	424	25704	99.57	$1^3T_{2u}$					
2	$T_{2u}$	2.316	424	25730	68.39	$1^3T_{2u}$	30.16	$1^1T_{2u}$			
2	$E_u$	2.315	422	26202	48.54	$1^1E_u$	25.35	$1^3T_{2u}$	25.02	$2^3T_{1u}$	
3	$T_{2u}$	2.314	422	26420	48.54	$1^3E_u$	23.19	$2^3T_{1u}$	21.10	$1^1T_{2u}$	
2	$T_{1u}$	2.314	423	26533	0.160	50.49	$1^3E_u$	21.19	$2^3T_{1u}$	15.29	$1^3T_{2u}$
1	$A_{1u}$	2.315	424	26664	96.37	$2^3T_{1u}$					
3	$T_{1u}$	2.316	421	27095	0.045	55.67	$2^3T_{1u}$	26.78	$2^1T_{1u}$		
3	$E_u$	2.315	422	28096	79.67	$2^3T_{2u}$	13.20	$2^3T_{1u}$			
4	$T_{2u}$	2.315	423	28327	48.35	$2^3T_{2u}$	29.41	$2^1T_{2u}$			
4	$T_{1u}$	2.316	421	28344	0.001	56.72	$2^3T_{2u}$	20.97	$2^1T_{2u}$	11.40	$2^1T_{1u}$
$4f^{13}(^2F_{5/2})5de_g$ submanifold; $\langle d_e \rangle = 2.316 \pm 0.001$ ; $\langle \omega_{a_{1g}} \rangle = 422 \pm 2$											
2	$A_{1u}$	2.317	424	34004	96.24	$1^3T_{1u}$					
5	$T_{1u}$	2.316	423	35075	0.797	51.63	$1^3T_{1u}$	21.10	$1^1T_{1u}$	16.08	$1^3T_{2u}$
4	$E_u$	2.315	423	35924	64.80	$1^3T_{2u}$	18.78	$1^1E_u$			
5	$T_{2u}$	2.315	423	36270	43.72	$1^1T_{2u}$	22.91	$1^3E_u$	20.02	$1^3T_{2u}$	
6	$T_{1u}$	2.316	421	36832	1.696	41.99	$1^3T_{2u}$	36.54	$1^1T_{1u}$	15.64	$1^3E_u$
5	$E_u$	2.315	422	37291	54.90	$2^3T_{1u}$	24.35	$1^1E_u$	19.89	$2^3T_{2u}$	
6	$T_{2u}$	2.315	423	37344	56.03	$2^3T_{1u}$	21.66	$1^3E_u$	14.64	$2^1T_{2u}$	
7	$T_{1u}$	2.315	416	38161	0.016	45.48	$2^1T_{1u}$	19.46	$1^3E_u$	16.83	$2^3T_{1u}$
Yb <sup>3+</sup> -doped CaF <sub>2</sub>											
$4f^{13}$ manifold; $\langle d_e \rangle = 2.201 \pm 0.001$ ; $\langle \omega_{a_{1g}} \rangle = 493 \pm 0$											
$4f^{13}(^2F_{7/2})$ submanifold											
1	$\Gamma_{7u}$ <sup>b</sup>	2.200	493	0	62.74	$1^2A_{2u}$	37.26	$1^2T_{2u}$			
1	$\Gamma_{6u}$	2.202	493	686	99.99	$1^2T_{1u}$					
1	$\Gamma_{8u}$	2.202	494	729	63.93	$1^2T_{2u}$	36.06	$1^2T_{1u}$			
$4f^{13}(^2F_{5/2})$ submanifold											
2	$\Gamma_{7u}$	2.201	494	10764	62.74	$1^2T_{2u}$	37.26	$1^2A_{2u}$			
2	$\Gamma_{8u}$	2.202	493	11196	63.94	$1^2T_{1u}$	36.06	$1^2T_{2u}$			

<sup>a</sup> Weights are given in % and correspond to calculations at  $d(\text{Yb-F}) = 2.200$  Å and  $2.383$  Å for  $\text{Yb}^{3+}$  and  $\text{Yb}^{2+}$  -doped  $\text{CaF}_2$ , respectively.

<sup>b</sup> The  $\text{Yb}^{2+} 1A_{1g} \rightarrow \text{Yb}^{3+} 1\Gamma_{7u}$  minimum-to-minimum energy difference is  $6905 \text{ cm}^{-1}$ .

TABLE II: Absorption and emission peak positions of the  $\text{Yb}^{2+}-\text{Yb}^{3+}$  pair in  $\text{CaF}_2$  and  $\text{SrF}_2$  calculated as total energy differences at the equilibrium geometries of the initial state.  $d_L$  and  $d_R$  are the Yb-F distances in the left and right  $\text{YbF}_8$  moieties. Only data referred in the text are given. For all vertical transitions and data in  $\text{BaF}_2:\text{Yb}^{2+}-\text{Yb}^{3+}$ , see Ref. 55. Experimental data are given in squared parentheses. Identification of calculated energy differences with absorption and emission transitions indicated in Figs. 4 and 8 are shown as roman numbers in parentheses. Energies in  $\text{cm}^{-1}$ , distances in Å. See text for details.

Final state $\text{Yb}^{2+}-\text{Yb}^{3+}$	$[4f^{14}, ^2F_{7/2}]$ $[1A_{1g}, 1\Gamma_{7u}]$ $d_L, d_R$		Yb <sup>2+</sup> -Yb <sup>3+</sup> initial state $[4f^{14}, ^2F_{5/2}]$ $[1A_{1g}, 2\Gamma_{7u}]$ $d_L, d_R$		$[^2F_{5/2}5de_g, ^2F_{7/2}]$ $[2A_{1u}, 1\Gamma_{7u}]$ $d_L, d_R$	
	CaF <sub>2</sub>	SrF <sub>2</sub>	CaF <sub>2</sub>	SrF <sub>2</sub>	CaF <sub>2</sub>	SrF <sub>2</sub>
	2.330,2.201	2.406,2.252	2.330,2.201	2.406,2.253	2.314,2.201	2.396,2.252
$[4f^{14}, ^2F_{7/2}]$			<b>(III<sub>em</sub>) Yb<sup>3+</sup> luminescence</b>			
$[1A_{1g}, 1\Gamma_{7u}]$	0	0	-10762	-10718	-33913	-34897
$[1A_{1g}, 1\Gamma_{6u}]$	686	580	-10078	-10140	-33226	-34316
$[1A_{1g}, 1\Gamma_{8u}]$	729	614	-10035	-10106	-33183	-34283
$[4f^{14}, ^2F_{5/2}]$						
$[1A_{1g}, 2\Gamma_{7u}]$	[10384] <sup>a</sup> 10763	10719	0	0	-23149	-24177
$[1A_{1g}, 2\Gamma_{8u}]$	[~10794] <sup>a</sup> 11196	11092			-22716	-23804
$\text{Yb}^{3+}-\text{Yb}^{2+}$ $[^2F_{7/2}, 4f^{14}]$					<b>(V) IVCT luminescence</b>	
					[-18200] <sup>b</sup>	
					[-18000] <sup>c</sup>	[-13700] <sup>c</sup>
					[-17400] <sup>d</sup>	[-12000] <sup>d</sup>
$[1\Gamma_{7u}, 1A_{1g}]$	15238	17894			-20508	-18121
$[1\Gamma_{6u}, 1A_{1g}]$	15728	18290			[-17600] <sup>b</sup>	
$[1\Gamma_{8u}, 1A_{1g}]$	15751	18307			-19999	-17716
					-19974	-17698
$\text{Yb}^{2+}-\text{Yb}^{3+}$ $[^2F_{7/2}5de_g, ^2F_{7/2}]$						
	[24814] <sup>e</sup>	[25316] <sup>e</sup>				
$[1E_u, 1\Gamma_{7u}]$	23576	24475				
$[1T_{2u}, 1\Gamma_{7u}]$	23614	24517				
$[1E_u, 1\Gamma_{6u}]$	24263	25055				
$[1T_{2u}, 1\Gamma_{6u}]$	24301	25097				
$[1E_u, 1\Gamma_{8u}]$	24305	25089				
$[1T_{2u}, 1\Gamma_{8u}]$	24344	25131				
	<b>(I) 1<sup>st</sup> photon absorption</b>					
	[27400] <sup>f</sup>	[27950] <sup>f</sup>				
$[1T_{1u}, 1\Gamma_{7u}]$	25706	26618				
others <sup>g</sup>						
$\text{Yb}^{3+}-\text{Yb}^{2+}$ $[^2F_{5/2}, 4f^{14}]$			<b>IVCT absorption</b>			
			[~ 28490] <sup>h</sup>			
$[2\Gamma_{7u}, 1A_{1g}]$	25922	28545				
$[2\Gamma_{8u}, 1A_{1g}]$	26243	28809				
others <sup>g</sup>						
$\text{Yb}^{2+}-\text{Yb}^{3+}$ $[^2F\ 5de_g, ^2F]$					<b>IR ESA<sup>i</sup></b>	
$[2A_{1u}, 1\Gamma_{7u}]$	34074	35003	23311	24284	0	0
					[250]	[178]
$[1E_u, 2\Gamma_{7u}]$	34340	35194	23576	24475	270	195
$[1T_{2u}, 2\Gamma_{7u}]$	34378	35236	23614	24517	307	236

	[ $2A_{1u}, 1\Gamma_{6u}$ ]	34761	35583	23996	24863	[650-950]	[500-670]
	[ $1E_u, 2\Gamma_{8u}$ ]	34772	35568	24007	24847	686	580
	[ $2A_{1u}, 1\Gamma_{8u}$ ]	34804	35617	24039	24896	702	568
	[ $1T_{2u}, 2\Gamma_{8u}$ ]	34810	35610	24045	24889	729	614
						739	609
	[ $5T_{1u}, 1\Gamma_{7u}$ ]	35145	36013	24382	25295	[1145]	[1273]
	[ $5T_{1u}, 1\Gamma_{6u}$ ]	35832	36594	25067	25873	1069	1013
Yb <sup>3+</sup> -Yb <sup>2+</sup>	[ $1\Gamma_{7u}, 1E_u$ ]					1756	1593
Yb <sup>2+</sup> -Yb <sup>3+</sup>	[ $5T_{1u}, 1\Gamma_{8u}$ ]	35874	36627	25109	25907	1775	
Yb <sup>3+</sup> -Yb <sup>2+</sup>	[ $1\Gamma_{7u}, 1T_{2u}$ ]					1799	1627
Yb <sup>2+</sup> -Yb <sup>3+</sup>	[ $4E_u, 1\Gamma_{7u}$ ]	36005	36927	25242	26208	1809	
	[ $5T_{2u}, 1\Gamma_{7u}$ ]	36356	37301	25593	26582	1917	1917
Yb <sup>3+</sup> -Yb <sup>2+</sup>	[ $1\Gamma_{6u}, 1E_u$ ]					2262	2292
	[ $1\Gamma_{8u}, 1E_u$ ]					2284	
	[ $1\Gamma_{6u}, 1T_{2u}$ ]					2309	
	[ $1\Gamma_{8u}, 1T_{2u}$ ]					2319	
						2343	
				(III) 2 <sup>nd</sup> photon absorption			
Yb <sup>2+</sup> -Yb <sup>3+</sup>	[ $1T_{1u}, 2\Gamma_{7u}$ ]	36470	37337	25706	26618	2343	2336
	others <sup>g</sup>						

<sup>a</sup> Only the absorption line at 10384 cm<sup>-1</sup> was assigned to a cubic site in Ref. 64; the splitting of the  $4f^{13}(^2F_{5/2})$  multiplet was expected to be similar to that found by Kiss (Ref. 67) for the isoelectronic ion CaF<sub>2</sub>Tm<sup>2+</sup>: 410 cm<sup>-1</sup>.

<sup>b</sup> From Ref. 6 and 7, below 200 K.

<sup>c</sup> From Ref. 8 at 77 K.

<sup>d</sup> From Ref. 11 at 4.2 K.

<sup>e</sup> Estimations from changes in the short time part of the fluorescence decay at 30 K, from Ref. 11.

<sup>f</sup> From absorption spectra from Ref. 6 and 7 at 20°C and Ref. 21 at 77 K.

<sup>g</sup> Ref. 55

<sup>h</sup> Read from Fig. 2 of Ref. 11; see text for details.

<sup>i</sup> Experimental data from two frequency transient photoluminescence enhancement spectra at 10 K, from Ref. 13 (CaF<sub>2</sub>) and Ref. 14 (SrF<sub>2</sub>).

TABLE III: Calculated diabatic energy barriers for the  $\text{Yb}^{2+}-\text{Yb}^{3+} \rightarrow \text{Yb}^{3+}-\text{Yb}^{2+}$  electron transfer reaction within the  $\text{Yb}^{2+}-\text{Yb}^{3+}$  active pairs in  $\text{CaF}_2$ ,  $\text{SrF}_2$ ,  $\text{BaF}_2$ , and  $\text{SrCl}_2$  fluorite-type crystals.  $[Di, Aj]$  and  $[Ak, Dl]$  are the electronic states of the pair before and after electron transfer. The energy barrier for crossing in the forward,  $[Di, Aj] \rightarrow [Ak, Dl]$ , and backwards,  $[Di, Aj] \leftarrow [Ak, Dl]$  reactions are given separated by a semicolon. The values of the Yb–X distances at the activated complex point,  $d_L, d_R$ , are given: they are, respectively, the Yb–X distances of the left (L) and right (R)  $\text{YbX}_8$  moieties. Energy barriers in bold format can be seen in Figures 4, 8, and 9, See text for details.

$(\text{YbX}_8)_L^{6-} + (\text{YbX}_8)_R^{5-} \rightarrow (\text{YbX}_8)_L^{5-} + (\text{YbX}_8)_R^{6-}$ $\text{Yb}^{2+}-\text{Yb}^{3+} \rightarrow \text{Yb}^{3+}-\text{Yb}^{2+}$ $[Di, Aj] \rightarrow [Ak, Dl]$	forward; backwards diabatic energy barriers for IVCT $d_L, d_R$ at the crossing point			
	$\text{CaF}_2$	$\text{SrF}_2$	$\text{BaF}_2$	$\text{SrCl}_2$
$[4f^{14}, 4f^{13}(7/2)] \rightarrow [4f^{13}(5/2), 4f^{14}]$ $[1A_{1g}, 1\Gamma_{7u}] \rightarrow [2\Gamma_{7u}, 1A_{1g}]$	11048; <b>285</b> 2.220, 2.311	11581; <b>862</b> 2.285, 2.377	12390; <b>1700</b> 2.349, 2.442	10837; <b>196</b> 2.711, 2.878
$[4f^{13}(7/2)5de_g, 4f^{13}(7/2)] \rightarrow [4f^{13}(5/2), 4f^{14}]$ $[1E_u, 1\Gamma_{7u}] \rightarrow [2\Gamma_{7u}, 1A_{1g}]$	<b>(II) crossing</b>			
$[1E_u, 1\Gamma_{7u}] \rightarrow [2\Gamma_{7u}, 1A_{1g}]$	<b>14</b> ; 12741 2.312, 2.205	<b>148</b> ; 13874 2.383, 2.266	<b>456</b> ; 15281 2.448, 2.322	<b>1826</b> ; 14375 2.880, 2.671
$[1T_{2u}, 1\Gamma_{7u}] \rightarrow [2\Gamma_{7u}, 1A_{1g}]$	10; 12775 2.313, 2.205	142; 13910 2.380, 2.263	453; 15323 2.446, 2.320	1847; 14433 2.882, 2.672
$[1T_{1u}, 1\Gamma_{7u}] \rightarrow [2\Gamma_{7u}, 1A_{1g}]$	49; 14903 2.323, 2.197	10; 15877 2.391, 2.255	166; 17164 2.460, 2.314	3400; 17963 2.903, 2.654
$[4f^{13}(7/2)5de_g, 4f^{13}(7/2)] \rightarrow [4f^{13}(7/2), 4f^{14}]$ $[1E_u, 1\Gamma_{7u}] \rightarrow [1\Gamma_{7u}, 1A_{1g}]$	<b>(IIq<math>n</math>ch) quenching</b>			
$[1E_u, 1\Gamma_{7u}] \rightarrow [1\Gamma_{7u}, 1A_{1g}]$	<b>1680</b> ; 25174 2.360, 2.159	<b>818</b> ; 25263 2.435, 2.222	<b>261</b> ; 25775 2.501, 2.278	9416; 32606 2.978, 2.612
$[1T_{2u}, 1\Gamma_{7u}] \rightarrow [1\Gamma_{7u}, 1A_{1g}]$	1701; 25229 2.364, 2.162	819; 25306 2.435, 2.222	266; 25825 2.504, 2.280	9425; 32652 2.978, 2.612
$[1T_{1u}, 1\Gamma_{7u}] \rightarrow [1\Gamma_{7u}, 1A_{1g}]$	2561; 28179 2.375, 2.154	1389; 27976 2.444, 2.212	570; 28256 2.510, 2.267	12846; 38050 3.025, 2.612
$[4f^{13}5de_g, 4f^{13}] \rightarrow [4f^{13}(7/2), 4f^{13}(7/2)5de_g]$ $[2A_{1u}, 1\Gamma_{7u}] \rightarrow [1\Gamma_{7u}, 1E_u]$	<b>76</b> ; 10570 2.306, 2.209	<b>385</b> ; 10909 2.367, 2.268	<b>912</b> ; 11470 2.433, 2.331	2838; 13393 2.914, 2.675
$[1E_u, 2\Gamma_{7u}] \rightarrow [1\Gamma_{7u}, 1E_u]$	55.5; 10818 2.308, 2.209	347; 11067 2.369, 2.268	878; 11567 2.434, 2.331	2853; 13494 2.916, 2.676
$[4f^{13}5de_g, 4f^{13}] \rightarrow [4f^{13}(5/2), 4f^{14}]$ $[2A_{1u}, 1\Gamma_{7u}] \rightarrow [2\Gamma_{7u}, 1A_{1g}]$	<b>1650</b> ; 24868 2.360, 2.160	<b>800</b> ; 25051 2.431, 2.220	<b>262</b> ; 25646 2.503, 2.280	9491; 32595 2.978, 2.612
$[1E_u, 2\Gamma_{7u}] \rightarrow [2\Gamma_{7u}, 1A_{1g}]$	1774; 25264 2.365, 2.162	861; 25307 2.436, 2.222	277; 25792 2.564, 2.241	9522; 32712 2.979, 2.612

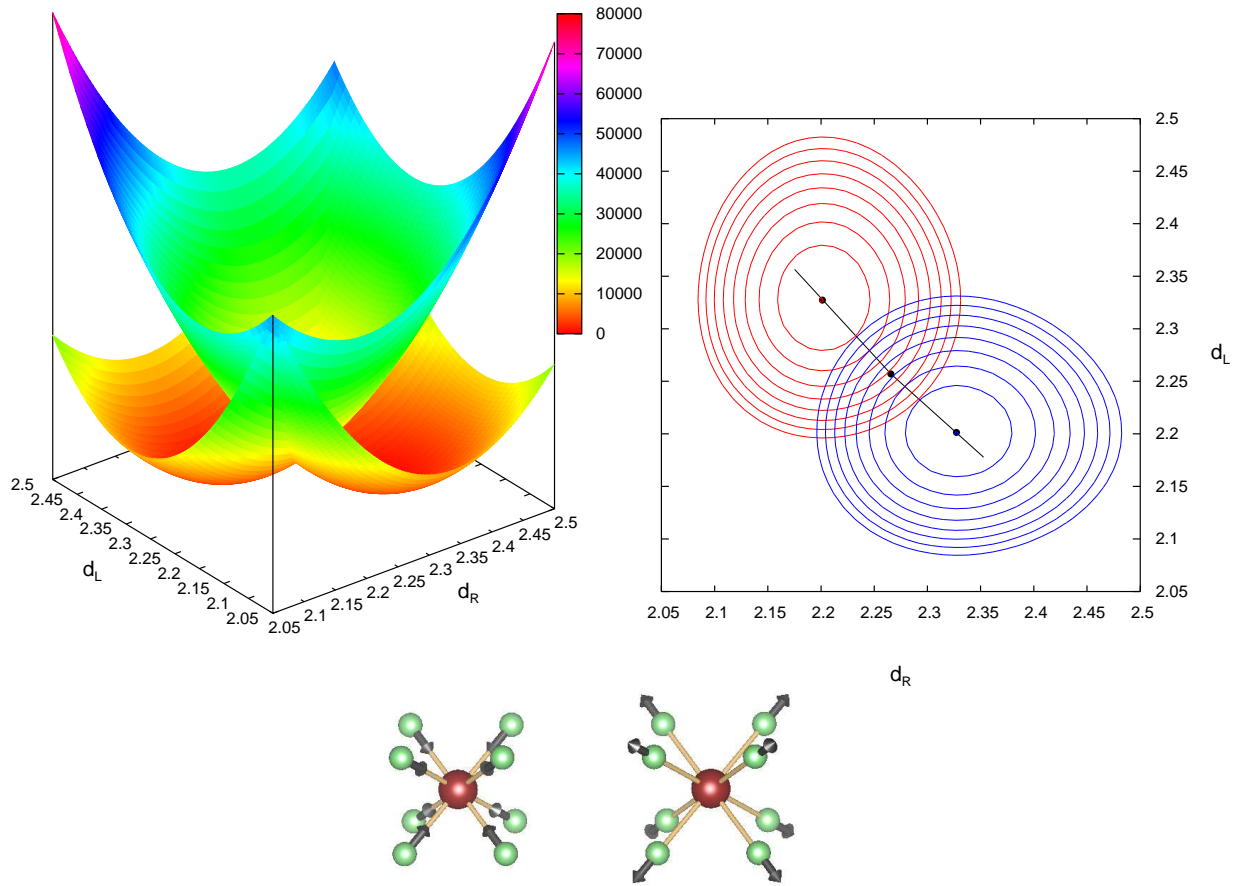


FIG. 1: Results of quantum mechanical calculations on Yb-doped  $\text{CaF}_2$  crystals. Top graphs: The two symmetric diabatic potential energy surfaces corresponding to the  $[1A_{1g}, 1\Gamma_{7u}]$  ground state of the  $\text{Yb}^{2+}-\text{Yb}^{3+}$  pair before  $(\text{YbF}_8)_L^{6-}-\text{Yb}^{3+}$   $[(\text{YbF}_8)_R^{5-}, 1A_{1g}, 1\Gamma_{7u}]$  (red in right graph) and after  $(\text{YbF}_8)_L^{5-}-\text{Yb}^{3+}$   $[(\text{YbF}_6)_R^{5-}, 1\Gamma_{7u}, 1A_{1g}]$  (blue in right graph) electron transfer are plotted (left graph) and projected (right graph) in the  $d_L, d_R$  plane. The Yb-F distances of the left ( $d_L$ ) and right ( $d_R$ ) moieties of the pair are given in  $\text{\AA}$ . Top left graph: Energies are given in  $\text{cm}^{-1}$  and are referred to the energy of the two equivalent ground state minima. Top right graph: The minimal energy reaction path connecting the two equivalent minima through the activated complex is indicated. Bottom graph: Displacements of the X atoms of the  $(\text{YbX}_8)_L-(\text{YbX}_8)_R$  moieties along the electron transfer reaction coordinate  $Q_{et}$ . See text for details.

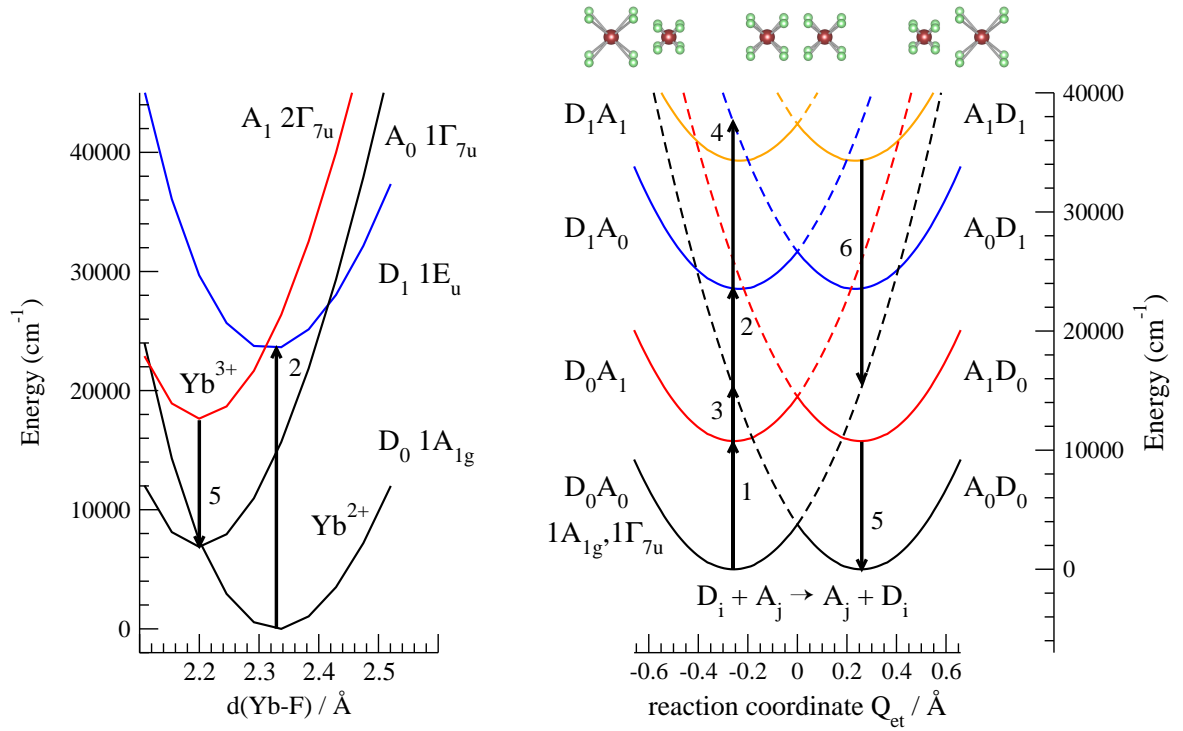


FIG. 2: Results of quantum mechanical calculations on Yb-doped CaF<sub>2</sub> crystals. Left graph: potential energy curves of the ground and one excited state of the independent (YbF<sub>8</sub>)<sup>6-</sup> and (YbF<sub>8</sub>)<sup>5-</sup> embedded clusters. Right graph: Diabatic IVCT energy diagram for Yb<sup>2+</sup>-Yb<sup>3+</sup> embedded pairs. The symmetric (YbF<sub>8</sub>)<sub>L</sub><sup>6-</sup>-(YbF<sub>8</sub>)<sub>R</sub><sup>5-</sup> D<sub>i</sub>A<sub>j</sub> and (YbF<sub>8</sub>)<sub>L</sub><sup>5-</sup>-(YbF<sub>8</sub>)<sub>R</sub><sup>5-</sup> A<sub>j</sub>D<sub>i</sub> branches are plotted vs. the normal electron transfer reaction coordinate Q<sub>et</sub> of the ground state. D<sub>i</sub> and A<sub>j</sub> refer to the parent independent embedded cluster states. Top right graph: Qualitative representations of the structure of the left and right moieties of the pair for Q<sub>et</sub> < 0, = 0 (activated complex), and > 0 are plotted. See text for details.

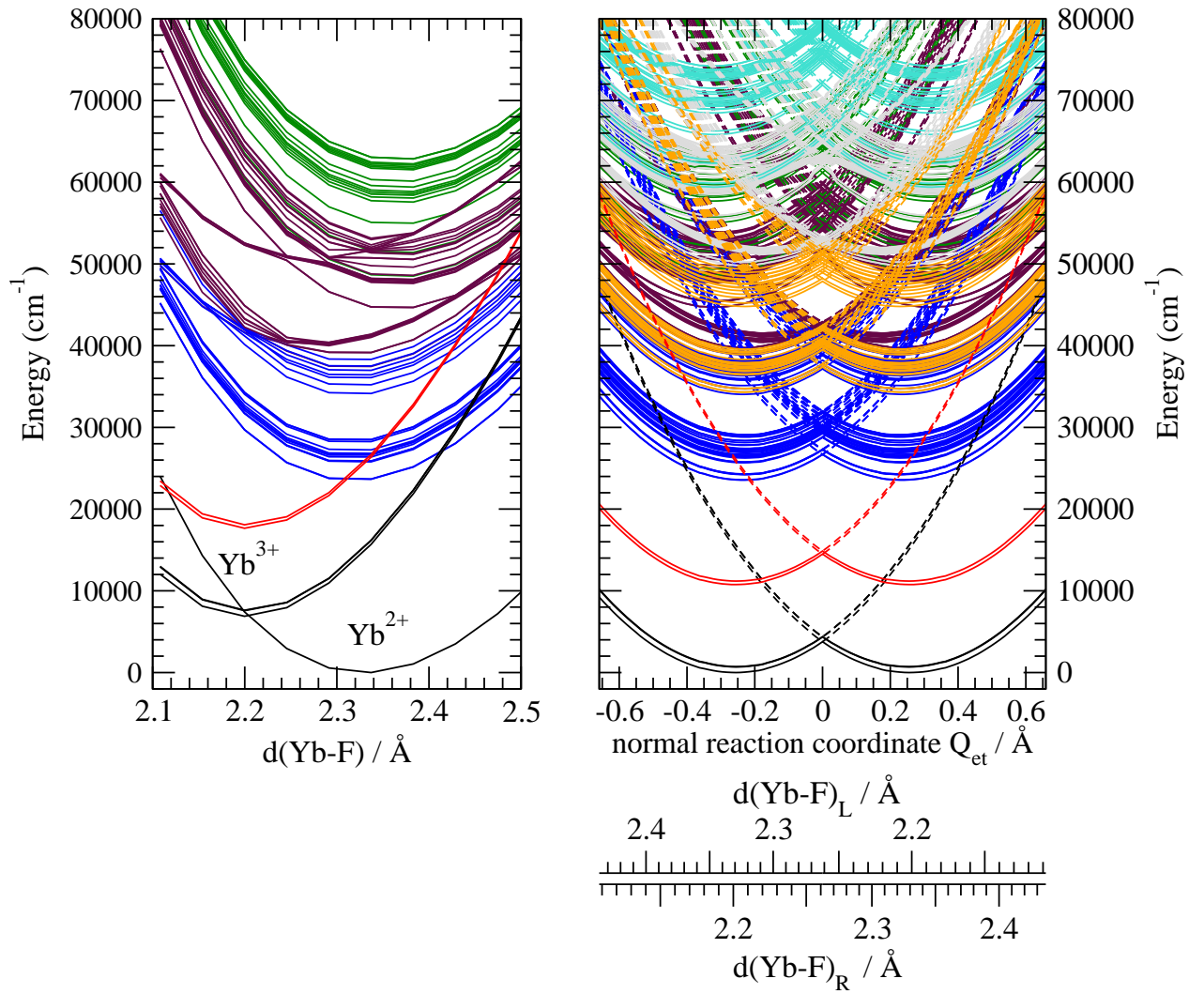


FIG. 3: Results of quantum mechanical calculations on Yb-doped  $\text{CaF}_2$  crystals. Left graph: potential energy curves of the ground and excited states of independent donor  $(\text{YbF}_8)^{6-}$  and acceptor  $(\text{YbF}_8)^{5-}$  embedded clusters. Right graph: Diabatic IVCT energy diagram for  $\text{Yb}^{2+}$ - $\text{Yb}^{3+}$  embedded pairs. The symmetric  $(\text{YbF}_8)_L^{6-}$ - $(\text{YbF}_8)_R^{5-}$  and  $(\text{YbF}_8)_L^{5-}$ - $(\text{YbF}_8)_R^{5-}$  branches of the ground and excited states of  $\text{Yb}^{2+}$ - $\text{Yb}^{3+}$  pairs are plotted vs. the normal electron transfer reaction coordinate  $Q_{et}$  for the pair ground state; the values of the Yb-F distance of the left and right  $\text{YbF}_8$  moieties,  $d_L$  and  $d_R$  are indicated. Colors in left graph: black  $4f^{14}$  and  $4f^{13}(7/2)$ ; red:  $4f^{13}(5/2)$ ; blue:  $4f^{13}5d_e$ ; maroon: interacting  $4f^{13}5d$  and  $4f^{13}a_{1g}^{\text{YbTE}}$ ; green:  $4f^{13}5dt_{2g}$  manifolds. Colors in right graph [ $\text{Yb}^{2+}, \text{Yb}^{3+}$ ]: black [ $4f^{14}, 4f^{13}(7/2)$ ], blue [ $4f^{13}5d_e, 4f^{13}(7/2)$ ], maroon [interacting  $4f^{13}5d$  and  $4f^{13}a_{1g}^{\text{YbTE}}, 4f^{13}(7/2)$ ], green [ $4f^{13}5dt_{2g}, 4f^{13}(7/2)$ ]; the four previous colours become red, orange, grey, and turquoise, when the  $\text{Yb}^{2+}$  states are combined with the  $\text{Yb}^{3+}$   $4f^{13}(5/2)$  states, instead.

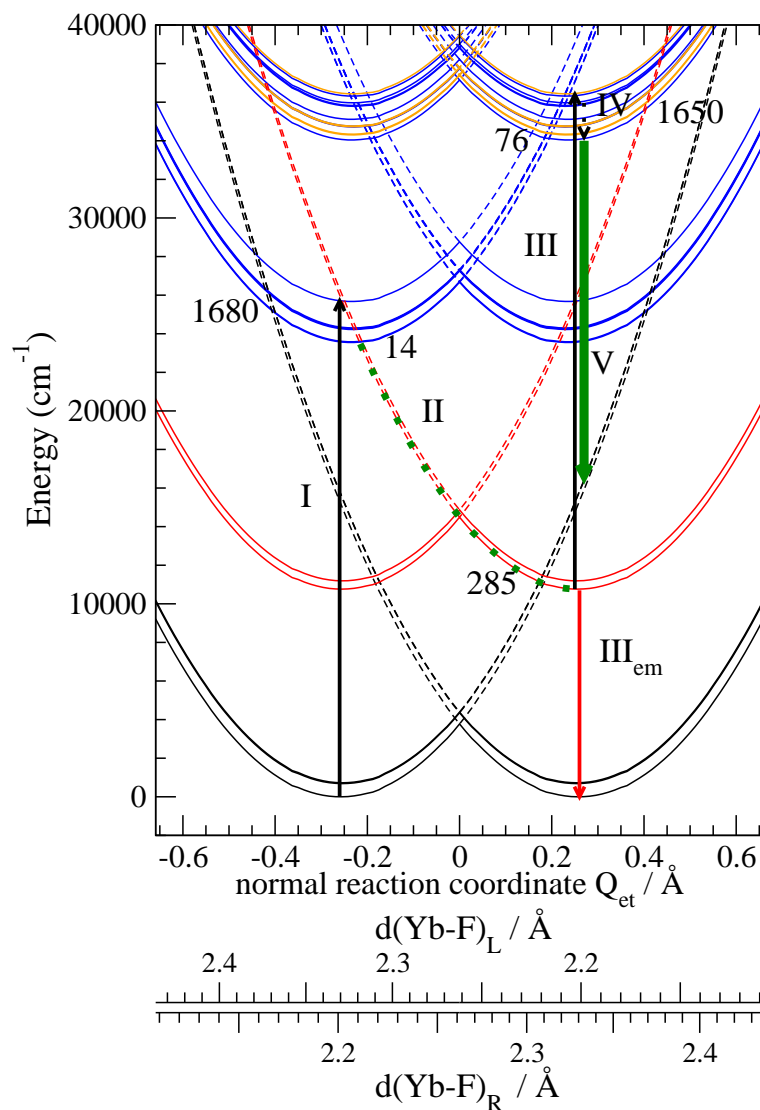


FIG. 4: Results of quantum mechanical calculations of the diabatic IVCT energy diagram for  $\text{Yb}^{2+}-\text{Yb}^{3+}$  pairs in Yb-doped  $\text{CaF}_2$  crystals along the ground state normal electron transfer reaction coordinate  $Q_{et}$ . Mechanism of the IVCT luminescence of Yb-doped  $\text{CaF}_2$  crystals: steps I to V. Mechanism of the excitation of the IR luminescence of  $\text{Yb}^{3+}$  through the lowest  $4f-5d$  absorption band of  $\text{Yb}^{2+}$ : steps I, II,  $\text{III}_{em}$ . Energy barriers in  $\text{cm}^{-1}$  are indicated next to the crossing points between two electronic states of the pairs; see details in Table III. See caption of Fig. 3 and text for details.



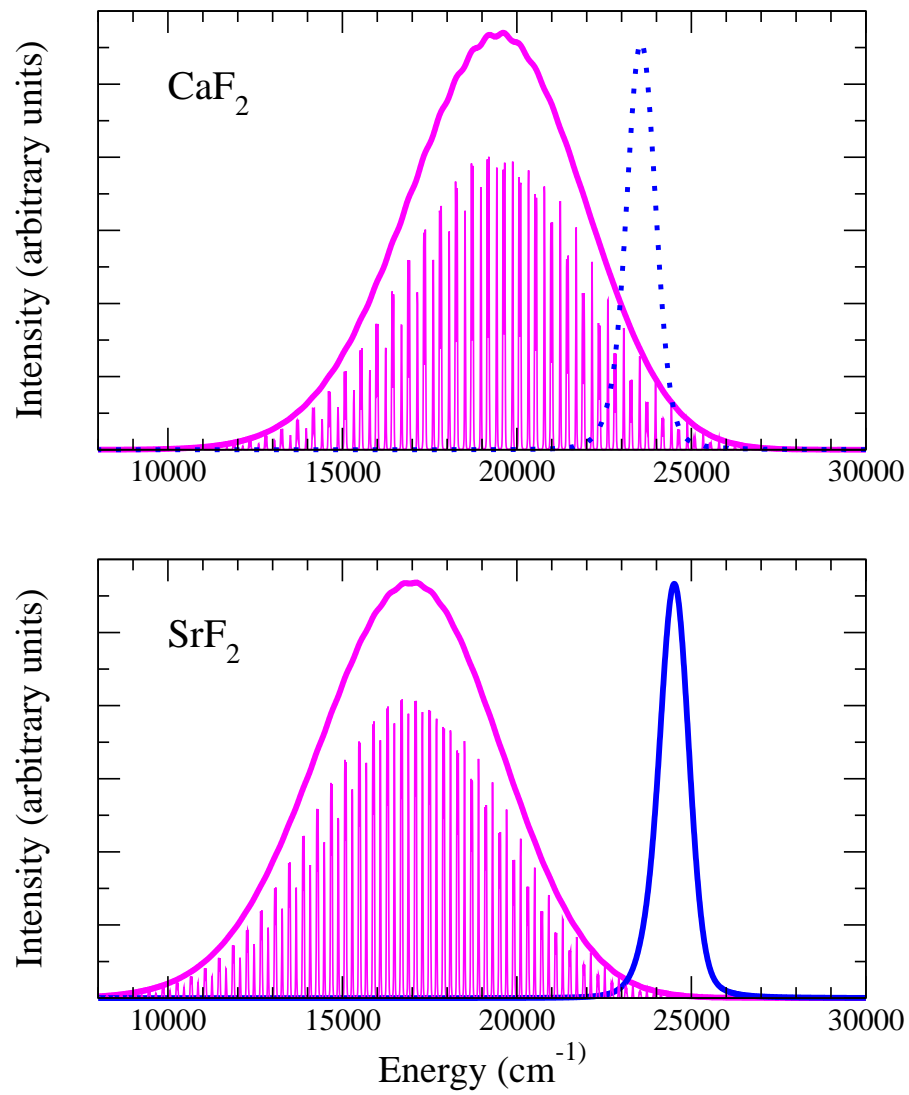


FIG. 5: Calculated band profiles of the  $\text{Yb}^{2+}-\text{Yb}^{3+} [2A_{1u}, 1\Gamma_{7u}] \rightarrow \text{Yb}^{3+}-\text{Yb}^{2+} [1\Gamma_{8u,6u,7u}, 1A_{1g}]$  intervalence charge transfer luminescence of  $(\text{YbF}_8)^{6-}-\text{(YbF}_8)^{5-}$  embedded cluster pairs (magenta) and of the  $1E_u \rightarrow 1A_{1g}$  emission band of embedded  $(\text{YbF}_8)^{6-}$  (blue) in  $\text{CaF}_2$  and  $\text{SrF}_2$ . Dotted line: not observable emission. Arbitrary values of the oscillator strengths have been used. See text for details.

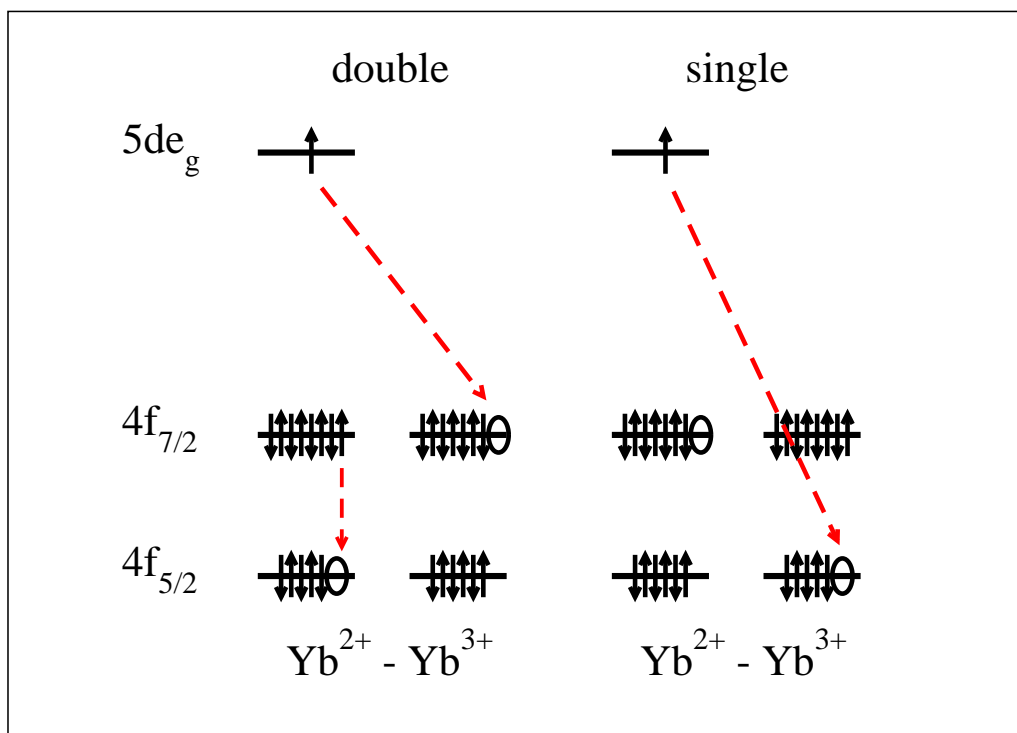


FIG. 6: Schematic representation of slow and fast IVCT emissions corresponding to a double deexcitation (double) consisting of an  $Yb^{2+} 5d_g \rightarrow Yb^{3+} 4f_{7/2}$  electron transfer accompanied by a  $4f_{7/2} \rightarrow 4f_{5/2}$  deexcitation within the  $4f^{13}$  subshell of  $Yb^{2+}$ ; and a single deexcitation (single) consisting of an  $Yb^{2+} 5d_g \rightarrow Yb^{3+} 4f_{5/2}$  electron transfer.

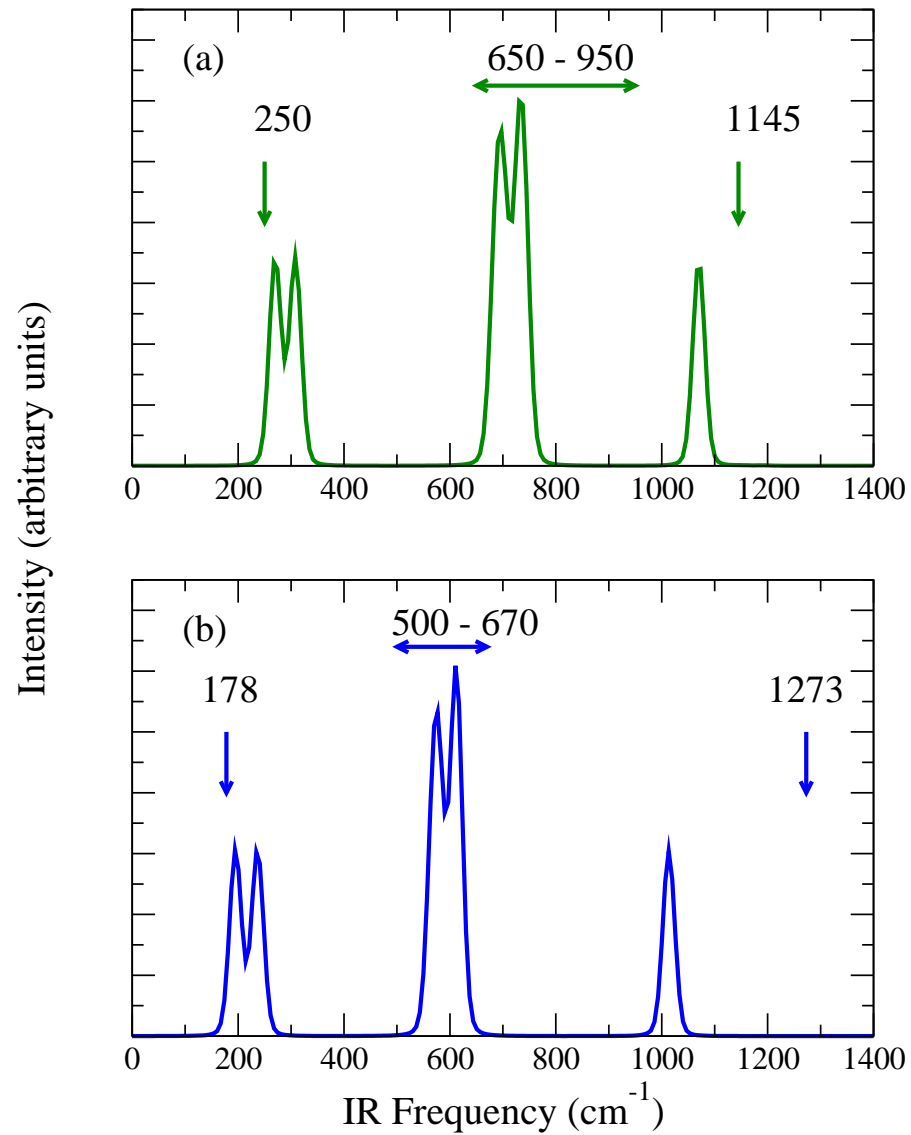


FIG. 7: Calculated excited state absorption spectrum of Yb-doped CaF<sub>2</sub> (a) and SrF<sub>2</sub> (b) originating in the Yb<sup>2+</sup>-Yb<sup>3+</sup> [ $2A_{1u}, 1\Gamma_{7u}$ ] excited state of the (YbF<sub>8</sub>)<sup>6-</sup>-(YbF<sub>8</sub>)<sup>5-</sup> embedded cluster pairs. Transition energies are taken from Table II. All transitions are arbitrarily assigned the same oscillator strength value. Experimental values from Ref. 13 (a) and 14 (b) are indicated with arrows.

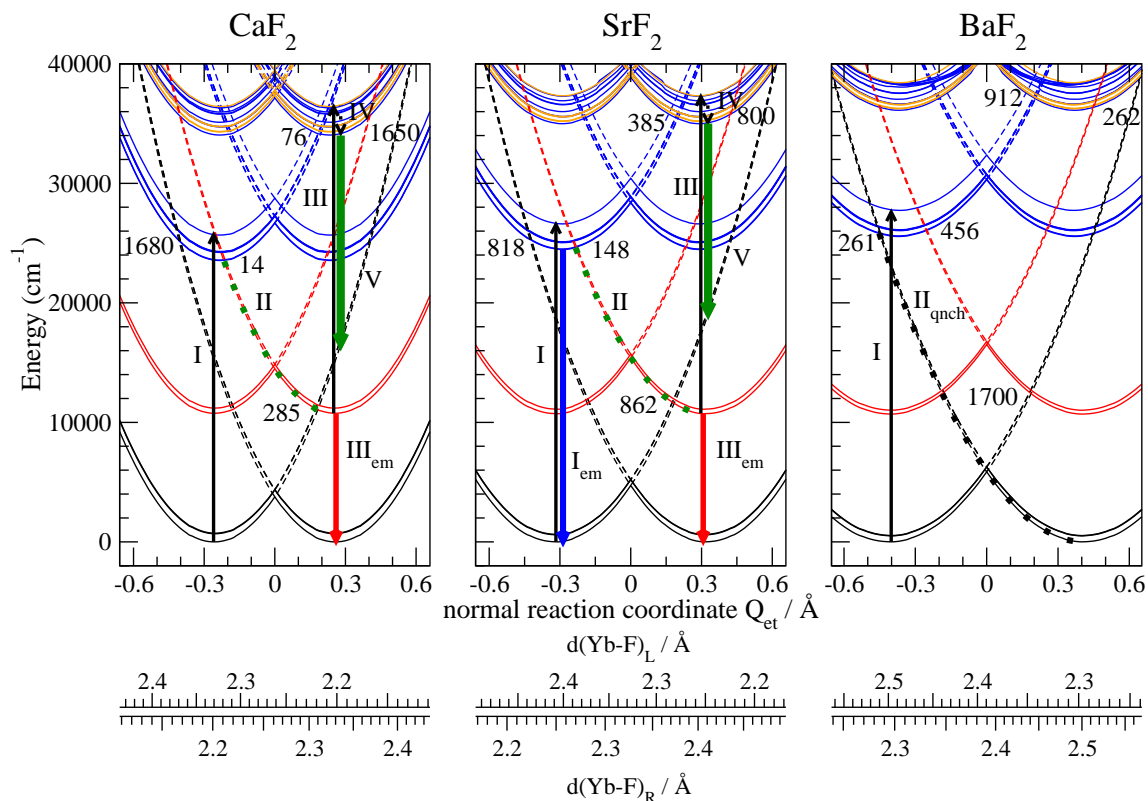


FIG. 8: Results of quantum mechanical calculations of the diabatic IVCT energy diagram for Yb<sup>2+</sup>-Yb<sup>3+</sup> pairs in Yb-doped CaF<sub>2</sub>, SrF<sub>2</sub>, and BaF<sub>2</sub> crystals along the ground state normal electron transfer reaction coordinate  $Q_{et}$ . CaF<sub>2</sub> and SrF<sub>2</sub>: IVCT luminescence: steps I to V; excitation of the IR luminescence of Yb<sup>3+</sup>: steps I, II, III<sub>em</sub>. BaF<sub>2</sub>: quenching of the Yb luminescence: Steps I and II<sub>qnch</sub>. Energy barriers in cm<sup>-1</sup> are indicated next to the crossing points between two electronic states of the pairs; see details in Table III. See caption of Fig. 3 and text for details.

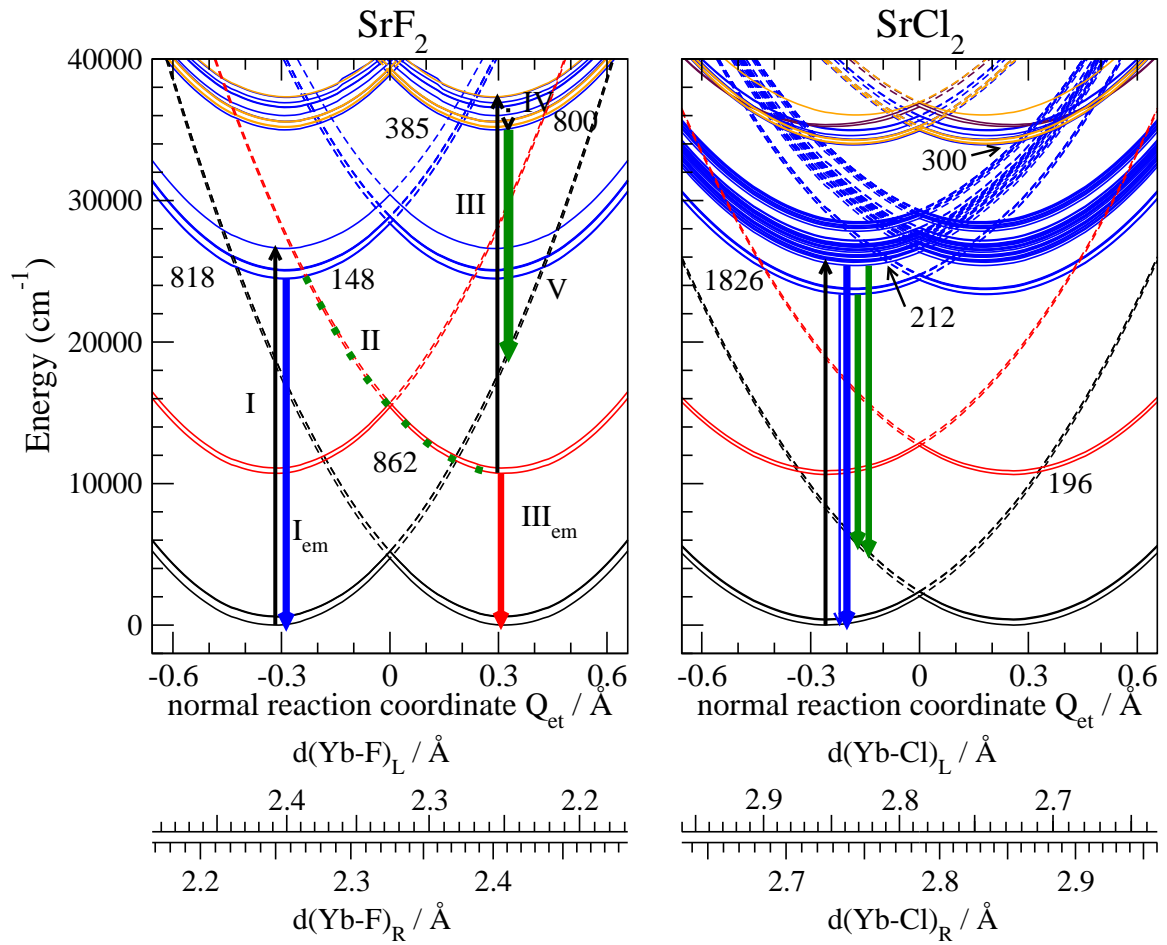


FIG. 9: Results of quantum mechanical calculations of the diabatic IVCT energy diagram for  $\text{Yb}^{2+}-\text{Yb}^{3+}$  pairs in Yb-doped  $\text{SrF}_2$ , and  $\text{SrCl}_2$  crystals along the ground state normal electron transfer reaction coordinate  $Q_{et}$ . IVCT luminescence in  $\text{SrF}_2$ : steps I to V; excitation of the IR luminescence of  $\text{Yb}^{3+}$ : steps I, II, III<sub>em</sub>; regular  $5d-4f$  emission: steps I, I<sub>em</sub>.  $\text{SrCl}_2$ : absorption (black),  $5d-4f$  emissions (blue) and IVCT emissions (green) are indicated by arrows. Energy barriers in  $\text{cm}^{-1}$  are indicated next to the crossing points between two electronic states of the pairs; see details in Table III. See caption of Fig. 3 and text for details.

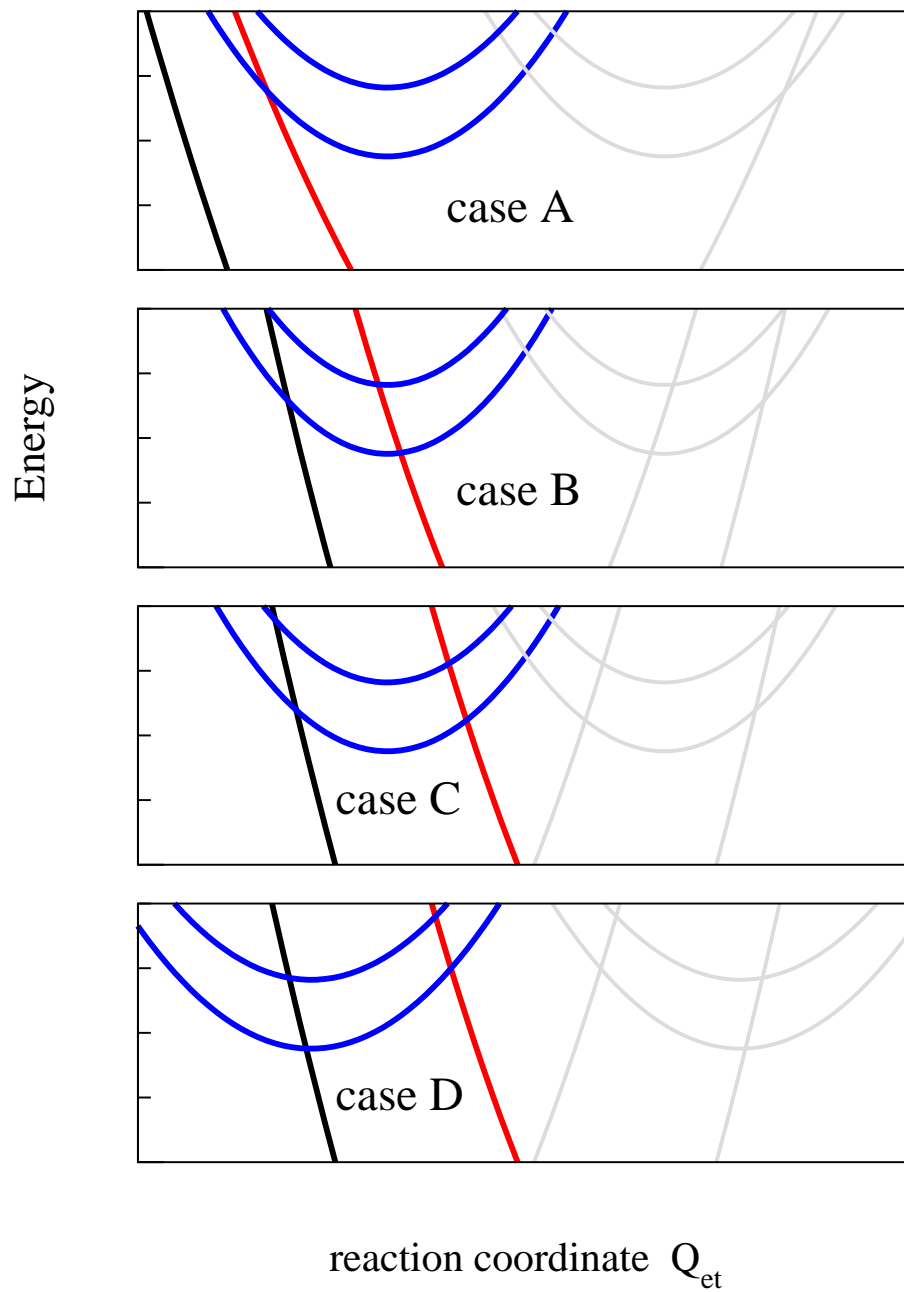


FIG. 10: Model cases for non-radiative electron transfer decays from  $\text{Yb}^{2+}\text{-Yb}^{3+}$  [ ${}^2F_{7/2}5de_g, {}^2F_{7/2}$ ] excited states (blue) in Yb-doped fluorite crystals determining the luminescence properties. Two non-radiative decay pathways leading to IVCT luminescence excitation (red) or to luminescence quenching (black) are emphasized.  $\text{Yb}^{2+}$ -doped  $\text{CaF}_2$  corresponds to case B,  $\text{SrF}_2$  to a case between B and C,  $\text{BaF}_2$ , to case D, and  $\text{SrCl}_2$  to case A.